2009

The dynamics of satellite disruption in cold dark matter haloes

JH Choi

MD Weinberg
weinberg@astro.umass.edu

N Katz
University of Massachusetts - Amherst, nsk@astro.umass.edu

Mon. Not. R. Astron. Soc. **000**, 000–000 (0000) Printed 17 August 2009 (MN LATEX style file v2.2)

The dynamics of satellite disruption in cold dark matter haloes

Jun-Hwan Choi⋆†, Martin D. Weinberg, Neal Katz

Department of Astronomy, University of Massachusetts, Amherst, MA 01003

17 August 2009

ABSTRACT

We investigate the physical mechanisms of tidal heating and satellite disruption in cold dark matter host haloes using N-body simulations based on cosmological initial conditions. We show the importance of resonant shocks and resonant torques with the host halo to satellite heating. A resonant shock (torque) couples the radial (tangential) motion of a satellite in its orbit to its phase space. For a satellite on a circular orbit, an ILR-like resonance dominates the heating and this heating results in continuous satellite mass loss. We estimate the requirements for simulations to achieve these dynamics using perturbation theory. Both resonant shocks and resonant torques affect satellites on eccentric orbits. We demonstrate that satellite mass loss is an outside-in process in *energy space*; a satellite's stars and gas are thus protected by their own halo against tidal stripping. We simulate the evolution of a halo similar to the Large Magellanic Cloud (LMC) in our Galactic dark matter halo and conclude that the LMC stars have not yet been stripped. Finally, we present a simple algorithm for estimating the evolution of satellite mass that includes both shock heating and resonant torques.

Key words: galaxies: evolution — galaxies: interaction — galaxies: haloes — galaxies: kinematics and dynamics — method: numerical — method: N-body simulation

1 INTRODUCTION

Physical processes affecting satellite galaxy evolution in their host haloes are an important component of galaxy formation in the cold dark matter (CDM) cosmogony as galaxies are built up from the assembly of small structures. This assembly includes the process of satellite galaxies merging with their host galaxies. Moreover, recent CDM cosmological simulations predict the existence of a large number of *subhaloes* (Ghigna et al. 1998; Klypin et al. 1999). Consequently, understanding the detailed physical processes affecting satellite evolution are key ingredients to understanding galaxy formation in the CDM cosmogony.

Several basic questions about satellite halo evolution remain. First, how is the satellite stripped? In other words, what parts of the initial mass distribution might persist to the present day? Second, what is the rate of satellite halo disruption? Third, how does a satellite's internal structure evolve? In a satellite-galaxy merger, the stars and gas of the satellite galaxy can be stripped and become halo stars and halo gas (e.g. Quilis et al. 2000; Bullock et al. 2001). The interaction between the satellite galaxy and its host during the course of the merger results in evolution of the satellite galaxy (e.g. Moore et al. 1996). The remaining components of the satellite galaxy merge with the host galaxy and this merging causes the host galaxy to gain mass (e.g. Murali et al. 2002).

Current cosmological simulations can only provide statistical properties of subhaloes since even in the highest resolution cosmological simulations (Ghigna et al. 2000; De Lucia et al. 2004; Diemand et al. 2004; Gao et al. 2004; Oguri & Lee 2004; Diemand et al. 2007; Springel et al. 2008) the detailed physical processes of individual subhalo evolution have not been accurately studied, owing to limited resolution. To investigate the physical processes in detail, we perform high resolution idealised simulations with cosmologically motivated initial conditions instead of using cosmological simulations. In these idealised simulations, a live satellite orbits in a static host halo. Although too simplified to reproduce a satellite's evolution in realistic detail, several authors have used similar non-cosmological simulations to study satellite disruption with alternative simulation methods (e.g. Hayashi et al. 2003; Kazantzidis et al. 2004; Read et al. 2006; Boylan-Kolchin & Ma 2007; Peñarrubia et al. 2008).

⋆ Current address : Department of Physics & Astronomy, University of Nevada, Las Vegas, 4505 S. Maryland Pkwy, Las Vegas, NV, 89154-4002
† Email: jhchoi@physics.unlv.edu

These studies have demonstrated important features of the satellite evolution such as mass loss history and density profile evolution. In this paper we use the higher resolution simulation to investigate satellite disruption particularly focusing on the detailed physical processes affecting satellite evolution such as resonant dynamics.

When a time-dependent force acts on a bound system such as a galaxy or a dark matter halo, resonant interactions play an important role in the system evolution. Recent studies of resonant dynamics in galaxy evolution claim that high resolution simulations are required to accurately reproduce these resonant effects (Weinberg & Katz 2007a,b) and Weinberg & Katz (2007a) provide a procedure to determine minimum particle number guidelines. Since our idealised, high resolution simulations are designed to satisfy these particle number guidelines, they allow us to investigate the role of resonant dynamics in satellite disruptions.

Resonant interactions couple a time-dependent perturbing force with orbits in the system. The frequency spectrum of the time-dependent perturbing force characterises the interaction. For a satellite orbiting in its host halo, the satellite's orbital frequencies, and possibly the rate of orbital decay, determine the time-dependence of the external force. A general, eccentric satellite orbit in a spherical halo has both a radial and azimuthal frequency, making the resonant coupling for an eccentric orbit complex. Empirically, we may characterise the overall effects of the interaction as a *resonant shock* and a *resonant torque*. A resonant shock represents coupling with the radial orbital frequency and a resonant torque represents coupling with the azimuthal orbital frequency.

A resonant shock is a generalisation of the standard impulsive, gravitational shock. During a resonant shock, some orbits within the satellite gain energy through resonant coupling even though they are not in the impulsive limit, i.e. the time scale of the perturbation near pericentre is much longer than the internal orbital time scale. A resonant torque couples the rotation in the external potential to orbits in the satellite. For a resonant torque, the magnitude of the external potential does not have to change; a change in the position angle of the satellite frame relative to the centre of the halo is sufficient to produce a torque. Resonant shocks have been previously considered and included in the impulsive approximation as an adiabatic correction (e.g. Spitzer 1987; Weinberg 1994a,b; Gnedin & Ostriker 1999). However, resonant torques have not been similarly considered in satellite evolution studies although they have been extensively investigated in the dynamics of barred galaxies. In this study, we will carefully investigate these resonant effects on satellite evolution using this distinction.

Globular cluster evolution in a host galaxy is well established (e.g. Spitzer 1987; Chernoff & Weinberg 1990). A globular cluster experiences both tidal truncation and heating by both compressive gravitational shocks and tidal shocks. Because satellite halo evolution in a host halo is similar to globular cluster evolution in a host galaxy, many galaxy formation studies employ simple analytic formulae taken from these globular cluster evolution studies to estimate satellite galaxy evolution. However, unlike globular clusters, the satellite–host mass ratio is *not* vanishingly small. This breaks the spatial symmetry in mass loss, as shown in Choi et al. (2007), and changes the relative importance of resonant coupling.

In this paper, we present numerical simulation results of satellite galaxy disruption. In §2, we present an overview of our numerical techniques: the N-body simulation code, the generation of initial conditions, and the relevant perturbation theory. In §3, we present the results of a circular orbit simulation. We show that resonant torque effects result in significant satellite mass loss. In §4, we present the results of eccentric orbit simulations. We show that satellite heating by gravitational shocks at pericentre, which also includes internal structure evolution, is the dominant process responsible for disrupting the satellite. In §5, we show that the process of satellite stripping is an outside-in process in satellite *energy* space. Using this finding, we suggest an explanation for the 'missing' LMC stellar stream. We also discuss the evolution of the satellite density profile. In §6, we provide an improved analytic estimate for satellite mass loss, and we summarise in §7.

2 NUMERICAL METHODS

Our N-body simulations use a three-dimensional self-consistent field code (SCF, also known as an expansion code; Clutton-Brock 1972, 1973; Hernquist & Ostriker 1992; Weinberg 1999). The expansion code calculates biorthogonal basis sets of density-potential pairs and computes the gravitational potential of the system using these basis sets. There are two reasons that an expansion code is an appropriate potential solver for our study. First, the expansion basis can be chosen to follow the structure over an interesting range of scales and simultaneously suppress small-scale noise. In contrast, the noise from two-body scattering can arise at all scales in direct-summation, tree, and mesh based codes. Small-scale noise can also give rise to diffusion in conserved quantities, which can then lead to unphysical outcomes particularly for studies of long-term galaxy evolution (Weinberg & Katz 2007a,b). Second, the expansion code is computationally efficient; the computational time increases only linearly with particle number and with modest overhead. Hence, the expansion code permits the use of a much larger number of particles than most other codes for the same computational cost.

The expansion code is not adaptive. The largest efficiency obtains when the basis resembles the galaxy. Otherwise, the expansion code requires a large number of basis function pairs, which introduces small-scale noise and results in a greater computational overhead. These constraints have been minimised by some recent improvements (Weinberg 1999; Choi et al. 2007). First, employing a numerical solution of the Sturm-Liouville equation, the initial galaxy model can be used as the zeroth-order basis function for the expansion code. Then, the expansion code requires only a modest number terms to accurately compute the potential. Second, we accurately trace the density–potential centre of the expansion during the course of a simulation (see Choi et al. 2007, for details). Third, to reduce truncation error, we separately track the centre of mass motion of the satellite and the relative motion of the satellite centre. With these improvements, the expansion simulations are now able to achieve a sufficiently high central resolution with suffi-

ciently low noise to allow the investigation of the detailed dynamical processes important for satellite disruption.

All the halo models used in our simulations are based on the cosmologically-motivated universal CDM halo (Navarro et al. 1997, hereafter NFW), $\rho(r) \propto r^{-1}(r+r_s)^{-2}$, where r_s is a scale length characterised by the concentration parameter $c = R_{vir}/r_s$ and R_{vir} is the virial radius of the halo. We represent the host halo potential by a concentration $c = 15$, static NFW halo. The NFW profile has infinite extent but a real satellite is tidally truncated. Furthermore, the host halo tidal field will affect a satellite halo even before the satellite halo passes within the host halo's virial radius, but it is computationally expensive to simulate the evolution of a satellite from such large radii. Since the objective of our study is only to understand the physical processes responsible for satellite disruption, it is not necessary to simulate the satellite's entire evolutionary history. Therefore, we begin the simulation with the satellite in the host halo on the desired orbit and include the host halo tidal field when we generate the satellite's initial conditions.

Our simulations ignore the effects of dynamical friction and the subsequent reaction of the host halo since the satellite masses of interest are often much smaller than that of the host halo. According to (Boylan-Kolchin & Ma 2007), when the satellite-to-host mass ratio is smaller than 0.1, the dynamical friction hardly makes the satellite decay within half a Hubble time. The gravitational back-reaction of the host halo has a complex structure with an amplitude proportional to mass ratio. In many cases, the halo reaction is dominated by barycentric motion of the halo center induced by the satellite perturbation. We will quantitatively discuss these dynamics in a later paper. Since our main objective in this paper is an understanding of the physical processes of satellite disruption, we do not expect omission of the halo response to affect our conclusions.

The details of the procedure that we use to generate a satellite's initial conditions are as follows. We start with an initial NFW satellite halo model. Since the maximum circular velocity is a better measure of a satellite's initial size than its mass, owing to ongoing mass loss, we characterise the satellite's size by its circular velocity $V = \sqrt{M_{vir}/R_{vir}}$. We choose the initial satellite halo model such that the circular velocity of the satellite $V_{sat} = \frac{1}{6}V_{host}$, which means that the initial virial mass of the satellite is 0.0046. Throughout this paper we use *system* units unless otherwise specified with $G = 1$, $M_{vir,host} = 1$, and $R_{vir,host} = 1$. If scaled to the Milky Way, this satellite halo corresponds to the size of the Sagittarius dwarf dark matter halo (Majewski et al. 2004). We then determine the truncation radius, for which we discuss several choices below, assuming that the satellite is on a circular orbit with $R = 0.4R_{host,vir}$. We call this fixed distance the tidal distance. As shown in Fig. 1a, the truncated model is identical to the initial NFW model but is chopped at the truncation radius. After truncating the initial satellite model at this radius, we perform an Eddington inversion to compute the corresponding distribution function (Binney & Tremaine 1987, Chapter 4), as shown in Fig. 1b. We calculate the final satellite density profile by integrating this distribution function over velocity. In contrast to the truncated model, the final satellite model does not show a sudden drop at the outer edge of its density profile (see Fig. 1c). Owing to this smooth outer profile, the final

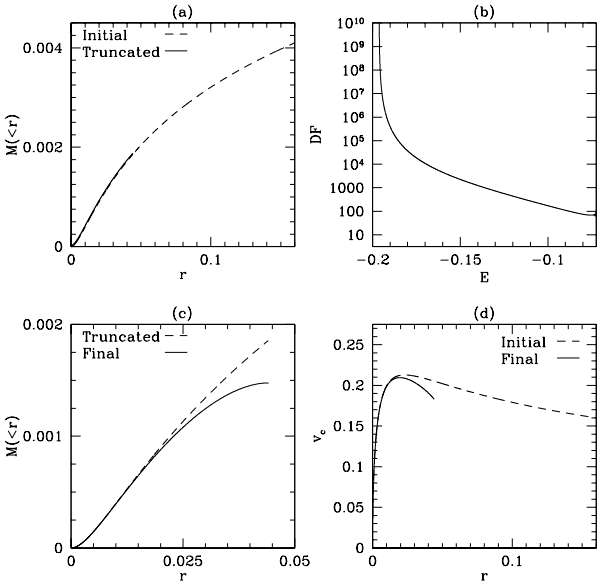

Figure 1. The effect of our truncation procedure on a satellite's initial NFW profile. (a) The density profiles of the initial NFW model and the truncated model. (b) The distribution function computed using Eddington inversion. (c) The density profiles of the truncated model and the final satellite model. (d) The circular velocity profiles of the initial NFW model and the final satellite model. The truncation radius in this figure is x_e and the satellite is on a circular orbit at $R = 0.4R_{vir}$.

satellite model is closer to equilibrium than the truncated model. We use this final satellite model as our initial satellite halo model. Fig. 1d shows the circular velocity profiles of the initial and final satellite model; even though the final satellite model is considerably truncated compared to the initial model and has lost 2/3 of its initial mass, the maximum circular velocities of both models are nearly the same. We realise the satellite phase space using an acceptance-rejection method. All realisations are assumed to have an isotropic velocity distribution and are made of 10^6 equal-mass particles.

The Roche limit, the critical-point radius x_e, and the tidal cut-off radius (r_t) (Spitzer 1987, Chapter 5) are all natural choices for the truncation radius. The Roche limit is the radius where the satellite density and the host halo density are the same. The critical-point radius, x_e, defines the unstable zero-velocity equilibrium; that is, the unstable equilibrium in the effective potential $d\Phi_{eff} = 0$. For ease in computing initial conditions and idealised tests in later sections, we define a *sphericised* centrifugal potential term of the form

$$\frac{1}{2}\Omega^2 \alpha r^2$$

with $\alpha \in [0, 1]$ (see Appendix A for details). For initial conditions, we set $\alpha = 1$ to make the satellite smaller and hence to minimise satellite mass loss owing to initial adjustments when it is first placed in the external potential. The tidal cut-off[1] is the radius where $r_t = 2x_e/3$. This is the radius of

[1] We follow Spitzer (1987) in defining the tidal cut-off radius

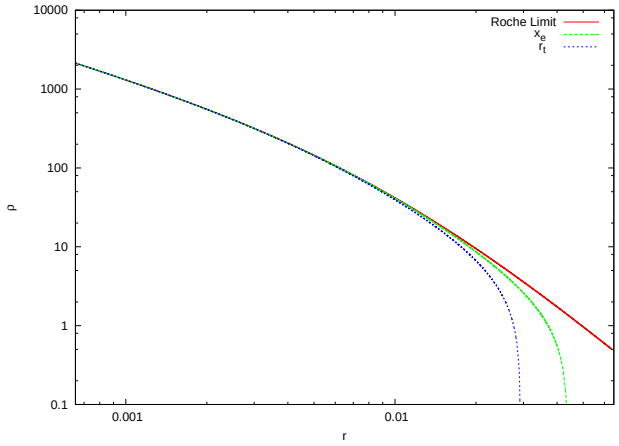

Figure 2. Density profiles for three satellite initial conditions truncated at three different radii: the Roche limit (red), x_e (green), and r_t (blue).

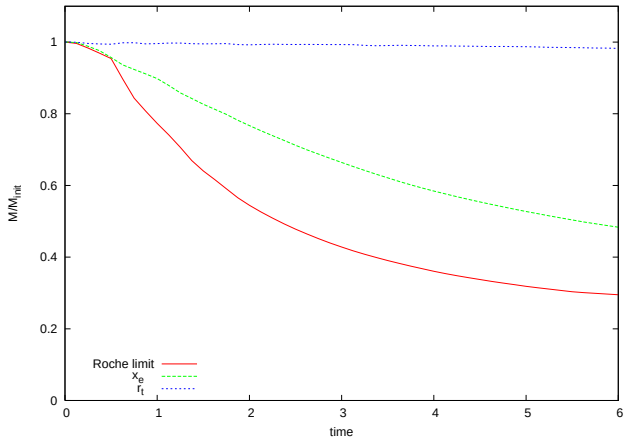

Figure 3. The evolution of fractional mass with time for satellites on circular orbits. Curves show the mass fractions remaining for satellites truncated at the Roche limit (red), x_e (green), and r_t (blue). All three simulations exhibit continuous mass loss. The satellite truncated at the Roche limit loses the most mass and the satellite truncated at r_t loses the least mass.

the critical potential surface perpendicular to the direction toward the host halo centre so it is the maximum radius that a spherical satellite halo can have and not extend beyond the critical potential surface in any direction. We plot the density profiles of the truncated satellite halo models in Fig. 2. To obtain the final density profiles for the satellite halo models truncated at x_e and r_t we apply the Eddington inversion procedure. However, we do not apply this procedure when we truncate at the Roche limit since it would change the outer density, making it differ from that of the host halo, and it would no longer be the Roche limit. Fig. 2 shows that at the given tidal distance of 0.4, the satellite truncated at the Roche limit is the largest and the satellite truncated at r_t is the smallest.

Fig. 3 shows the evolution of mass from circular orbit simulations for the three satellites shown in Fig. 2 (see §3 for a detailed discussion). All three satellites show continuous mass loss. The amount of mass loss correlates with the satellite size: the satellite truncated at the Roche limit loses the largest mass fraction and the satellite truncated at r_t loses the least mass. We choose x_e for our fiducial truncation radius on physical grounds. x_e is the transition point beyond which satellite particles on a circular orbit become unbound. At the Roche limit radius for an NFW halo, the host halo potential dominates the gravitational potential of the satellite. In contrast, using the tidal cut-off radius, r_t, is a sensible choice for globular clusters, which have already orbited many times around a galaxy and have already been severely truncated, but using r_t could underestimate a satellite halo's size since it has made only a few complete orbits. Hence, we restrict our study to initial satellite haloes that are truncated at x_e.

As mentioned in §1, resonant interactions are expected to dominate the tidal heating. To accurately reproduce these resonant interactions, N-body simulations need to satisfy several numerical criteria. Weinberg & Katz (2007a) proposed explicit requirements for these criteria. First, a sufficient number of particles are required to cover the phase space near resonance (hereafter, the *coverage* criterion). Second, a sufficient number of particles are required to reduce artificial diffusion. Artificial diffusion can come from both the gravitational forces of individual particles (hereafter, the *small-scale noise* criterion) and the potential fluctuations caused by Poisson noise (hereafter, the *large-scale noise* criterion). Besides these particle number criteria, the potential solver must also be able to resolve the scale of the resonant potential and the realised phase space distribution must cover this region. In our study, we will verify that our simulations satisfy all of these criteria.

Although a simulation can correctly reproduce resonant interactions, it is hard to provide a detailed accounting of the individual resonances. For intuitive guidance, the resonant interaction effects can be investigated using perturbation theory. We use a numerical perturbation theory calculation as in Weinberg & Katz (2007a) to investigate resonant interaction effects. In this approach, one begins with the numerical integration of the perturbed orbit-averaged Hamilton equations in a fixed potential for the entire phase space. This step may be followed by an update of the gravitational potential. Since this perturbation calculation uses the same satellite halo realisation, comparison with the N-body simulation result is straightforward. A comparison between the results of the N-body simulation and those of the numerical perturbation theory calculation provides us with strong evidence for the existence of resonant dynamics and a definite understanding of its role in satellite evolution.

3 SATELLITE DISRUPTION ON A CIRCULAR ORBIT

To study the resonant torque effect in isolation, we simulate a satellite on a circular orbit, which eliminates the gravitational shock. However, as long as the satellite's rotation does not match its orbital rotation, i.e. it is not *tidally locked*, the

as that derived for point-mass potentials with vanishingly small satellite masses to avoid any further confusion in terminology. For extended gravitational potentials, the numerical value will differ from 2/3.

satellite will experience a time-dependent azimuthal force variation that can result in a net resonant torque.

3.1 Investigation of the resonance torque effect

As described in Fig. 3, satellites on a circular orbits continuously lose mass and have lost a significant fraction of their original mass at the end of the simulation (approximately the age of the Universe). If a transient adjustment of the satellite halo to its host halo potential were the cause of the mass loss, the mass loss should lessen and stop in several dynamical times as the satellite adjusts to the halo potential. Therefore, continuous mass loss from truncated satellite haloes must result from satellite heating and not from a transient initial adjustment. In a circular orbit simulation, the magnitude of the external potential does not vary and, therefore, there is no gravitational shock. The only mechanism that can disrupt a satellite under these circumstances is a resonant torque.

The dynamics of the resonant torque are similar to the dynamics of the bar-halo interaction. Owing to the coupling with the time-dependent perturbation, the orbits whose frequencies are nearly commensurate with the perturber's frequency are torqued. The commensurability condition is

$$l_1\Omega_1 + l_2\Omega_2 = l_3\Omega_{pert} \quad (1)$$

where Ω_1 and Ω_2 are the radial and azimuthal frequencies of a satellite's orbit, Ω_{pert} is the perturber's frequency, and l_1, l_2, and l_3 are integers. The orbits that satisfy equation (1) are called *resonant* orbits and define loci in phase space for each triple of integers $l_1 : l_2 : l_3$. The resonant torque heats the satellite, reduces the satellite's binding energy, and enhances its mass loss. Although particular resonant orbits receive or lose angular momentum, mass loss is not confined to the resonant orbits. Since a satellite is a self-consistent gravitational system, the work required to apply the torque reduces the entire satellite's binding energy and unbinds the most weakly bound halo material. Satellite mass loss in general will be discussed in §5.

Perturbation theory calculations provide helpful physical insights into the nature of these resonant dynamics. The angular momentum transfer by the resonant interactions may be approximated by a second-order, time-dependent perturbation calculation (Weinberg 2004; Weinberg & Katz 2007a,b). These calculations become prohibitively complicated for real astronomical systems with multiple time scales. First, owing to the finite age of the galaxy and the time-dependence of the perturbation, the frequency spectrum becomes broader. Secondly, some resonances need a longer time period than the galaxy lifetime to converge into the time-asymptotic limit and, in the interim, the first-order transient features may strongly affect the response. More detailed discussions of perturbation theory and resonant dynamics are presented elsewhere (Tremaine & Weinberg 1984; Weinberg 2004; Weinberg & Katz 2007a,b). For our calculations here, we represent the host halo potential by an orbiting perturber around a stationary satellite with the distance of the perturber to the satellite equal to the distance between the satellite and the host halo centre in the simulation. The mass of the perturber is the enclosed mass of the host halo inside the satellite's orbit in the simulation, and the perturber's frequency is the same as the satellite's

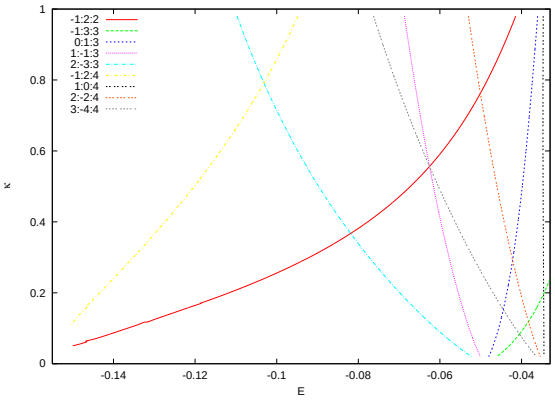

Figure 4. The locations of resonances within the satellite in energy-angular momentum space. The low-order resonances with $-10 \leq l_1 \leq 10$ and $l = 1, 2, 3, 4$ are shown (see text for details).

orbital frequency. We investigate the resonant torque using the following three steps: (1) we find the resonances that are located within the satellite, (2) we estimate the particle number requirements for a given resonance using the criteria from Weinberg & Katz (2007a), and (3) we compute the individual resonant effects using a numerical perturbation theory calculation and compare them to the simulations.

Fig. 4 shows the locations of the resonances within the satellite phase space. The phase space location is represented by energy (E) and normalised angular momentum[2] (κ). The range of resonances we examine is $-10 \leq l_1 \leq 10$ and we restrict ourselves to $l = 1, 2, 3, 4$, where l is the spherical harmonic of the perturber, in this case the primary galaxy. Owing to symmetry, l_2 and $|l_3|$ should be equal to or less than l. Since l_2 and l_3 are indices of the azimuthal expansion in spherical harmonics for the halo and perturber respectively, l_2 and l_3 should have the same parity as l (Tremaine & Weinberg 1984). As one can see in Fig. 4, nine resonances are located within the satellite.

The required numbers of equal mass particles within our truncated satellite for the four strongest resonances are presented in Fig. 5. There are three particle number criteria for each resonance: coverage, small-scale noise, and large-scale noise (Weinberg & Katz 2007a). According to this estimate, we require more than 10^5 satellite particles, which translates to more than 3×10^5 within the initial virial radius, to correctly reproduce the -1:2:2 resonance. This resonance requires the largest number of particles and is also the most important resonance as we show below. Hence, our 10^6 equal-mass particle halo simulation easily satisfies the necessary criteria (see Fig. 5) for all the important resonances. The small-scale noise criterion is not relevant for our expansion-code simulations. However, if the N-body simulations were to suffer from small-scale noise, such as the case in N-body simulations using direct-summation, trees, or meshes, an order of magnitude larger particle number would be required for these resonances to be modelled correctly.

[2] The quantity $\kappa \equiv J/J_{max}(E)$ where J is a particle's angular momentum and $J_{max}(E)$ is the maximum angular momentum at a given energy.

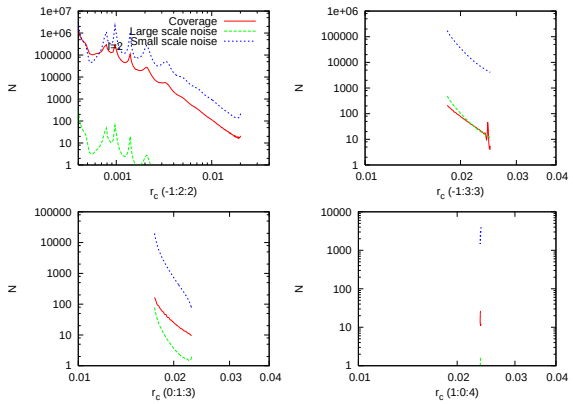

Figure 5. Particle number requirements for the -1:2:2, -1:3:3, 0:1:3, and 1:0:4 resonances. These are the strongest four resonances for a satellite on a circular orbit. Each panel shows the three particle number requirements from Weinberg & Katz (2007a) for equal mass particles within the initial truncated satellite. They are plotted versus r_c, the radius of a circular orbit of a given energy in units of the host's virial radius.

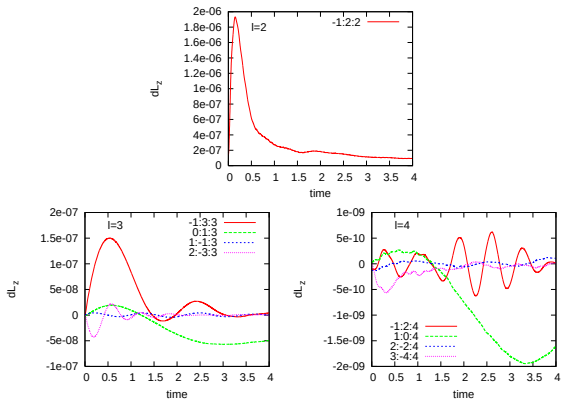

Figure 6. The angular momentum transferred from the perturber to the satellite as function of time. The panels show the $l = 2, 3, 4$ contributions as labelled. The -1:2:2 resonance (top panel) dominates the torque.

Fig. 6 shows the amount of angular momentum deposited by an orbiting perturber calculated using numerical perturbation theory for different resonances. The most significant angular momentum change is mediated by the -1:2:2 resonance. The -1:3:3 and 0:1:3 resonances are the strongest among the $l_3 = 3$ resonances, and the 1:0:4 resonance is the strongest resonance among the $l_3 = 4$ resonances. The amount of angular momentum deposited by the -1:2:2 resonance is more than an order of magnitude larger than the amount of angular momentum deposited by any of the $l_3 = 3$ resonances and three orders of magnitude larger than the amount of angular momentum deposited by any of the $l_3 = 4$ resonances. Hence, the -1:2:2 resonance dominates the resonant satellite torque.

Fig. 7 shows the location of the angular momentum transferred through resonant interactions in phase space by plotting the distribution of the change in L_z in phase space, ΔL_z, at different times from both the N-body simulation and the numerical perturbation theory calculation. We normalise this change by the total angular momentum at each energy E since $L(E)$ at fixed κ increases with energy, which biases the absolute ΔL_z distribution toward higher energies. By normalising to the total angular momentum at a given energy bin, the *relative* ΔL_z distribution enhances ΔL_z features at low energy. Each panel shows the relative ΔL_z over a fixed time span. Both the phase space location and magnitude of the angular momentum change from the simulation agrees well with the numerical perturbation calculation. The perturbation theory only includes the resonant torque and therefore this agreement is strong evidence that torque by resonant interactions is the major mechanism responsible for circular orbit satellite evolution.

Nonetheless, some minor discrepancies remain. First, the amplitude of the relative ΔL_z from the perturbation calculation is larger than that from the simulation at T =0.0–1.0. This results from the abrupt introduction of the perturbation. In our calculations, we abruptly introduce the external potential (for the simulation) and perturbations by resonances (for the perturbation calculation) to the initial satellite. This abrupt introduction may induce a readjustment of satellite halo equilibrium and/or cause non-linear features, which could cause the discrepancy. Second, the shape of the region of angular momentum change is mildly different in the simulation compared to the perturbation calculation. In particular, the simulation shows a relative ΔL_z distribution in the lower right region of phase space, while the perturbation calculation does not. The phase space responsible for this difference in the ΔL_z distribution has low binding energy and is easily stripped. The simulation results in Fig. 7 shows the distribution of the relative ΔL_z for only the unstripped particles. Unlike in the simulations, the satellite in the perturbation calculation does not lose mass. Hence, the few minor disagreements between the simulation and the perturbation theory are a natural consequence of the idealisation required to compute the perturbation theory and does not invalidate our primary conclusion: resonant torque is the major mechanism responsible for satellite disruption for a satellite on a circular orbit.

The absence of a $l = 1$ resonance contribution is a consequence of satellite truncation. Roughly, the tidal radius of the satellite coincides with the corotation radius of the satellite since $\Omega_{pert} \sim \Omega_2$ at r_t. The satellite halo is isotropic so $|\frac{\Omega_{pert}}{\Omega_2}| < 1$ and it follows from equation (1) that $|l_1 \frac{\Omega_1}{\Omega_2} + l_2| < 1$ for a resonance within the satellite. Since Ω_1/Ω_2 is always larger than 1, $|l_1 \frac{\Omega_1}{\Omega_2} + l_2|$ has its lowest value when $l_1 = 1$ and $l_2 = -1$, making the location of the 1:-1:1 resonance outside of the satellite. Hence, if the satellite is tidally truncated there is no $l = 1$ resonance contribution to satellite disruption.

3.2 Verifying mass loss by the resonant torque

The simulation results and the perturbation theory calculation agree on the amplitude and phase space location of the angular momentum exchange, which confirms the importance of the resonant torque. However, there is another process that may cause mass loss: re-equilibration of the satellite after some particles are tidally stripped by the host halo potential. This readjustment in the profile forces some particles to move beyond the tidal radius and also results in continuous mass loss. In our simulation, the satellite initial

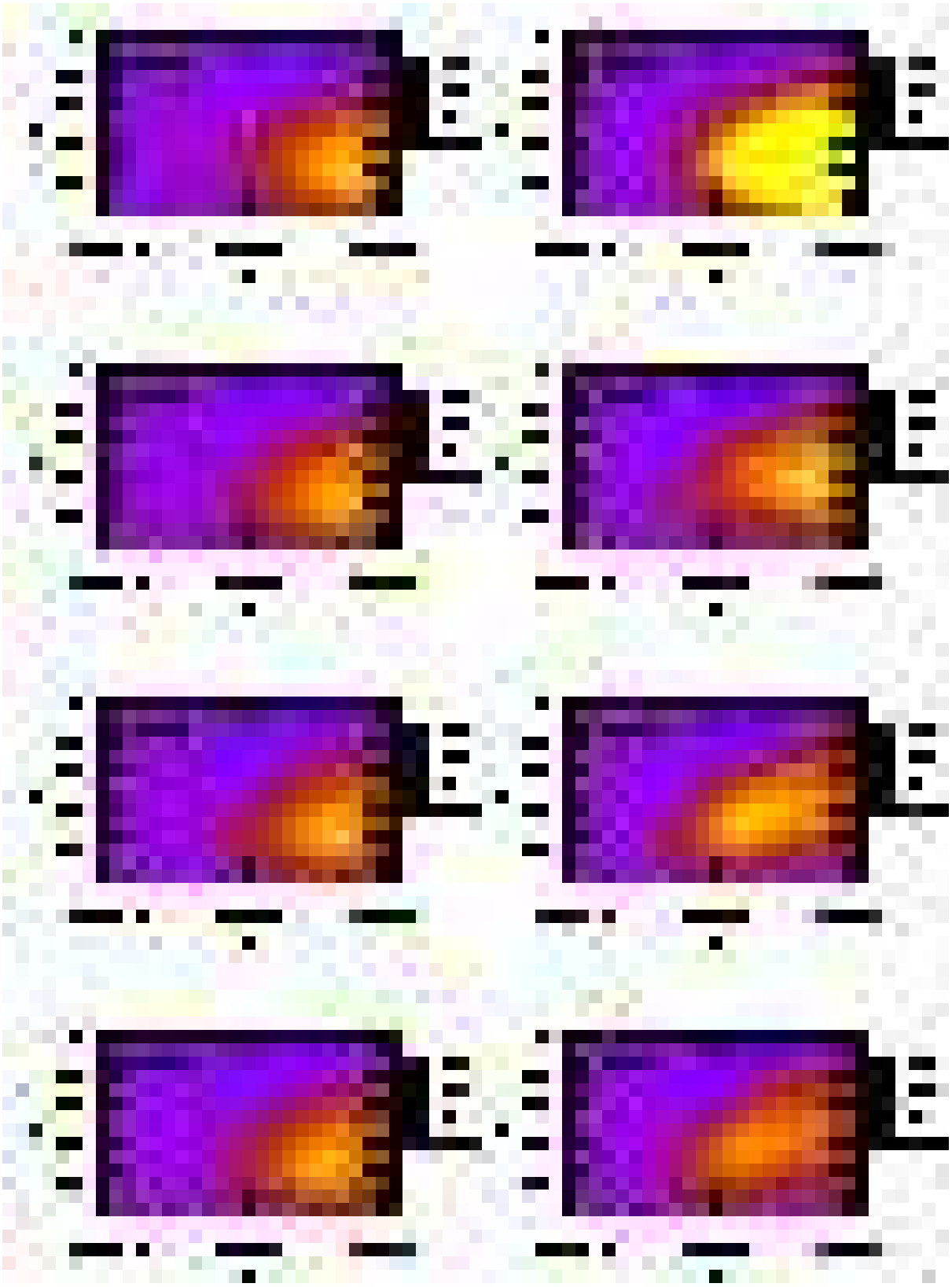

Figure 7. The distribution of the relative change in L_z in phase space for the N-body simulation (left panels) and the numerical perturbation theory calculation (right panels) The perturbation theory calculation includes all the resonances in Fig. 4. Except for $T = 0.0 - 1.0$, the results show good general agreement. This agreement provides robust evidence for resonant effects in the circular orbit simulation.

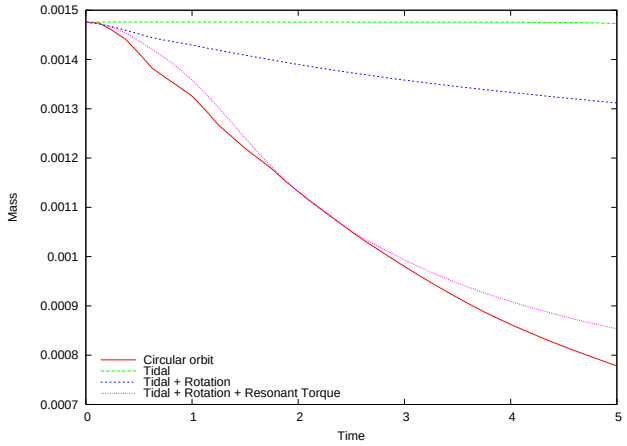

Figure 8. The mass loss histories from the synthetic force experiments (see text).

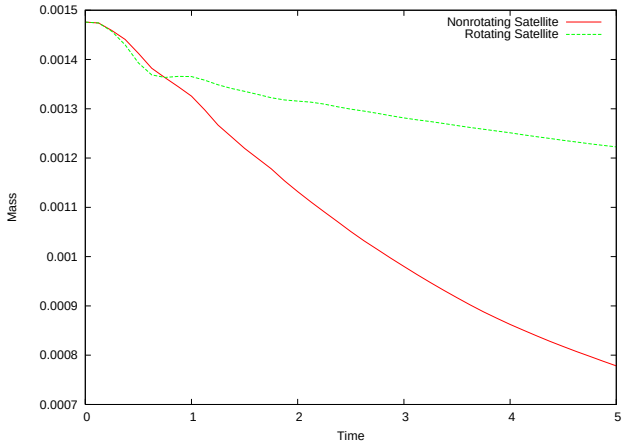

Figure 9. The mass loss history of circular orbit simulations for both a non-rotating and a rotating satellite. Since the rotating satellite simulation suppresses the resonant torque, its mass loss is significantly reduced.

conditions are designed to reduce the mass lost through this process by truncating satellites at the tidal radius but, owing to the Eddington inversion, a small amount of mass loss is inevitable. To elucidate the affect of resonant torque on satellite mass loss, we conduct two types of idealised numerical experiments. In the first, we add angular momentum to the simulation using the torque determined from perturbation theory, tidal truncation, and the centrifugal and Coriolis forces. We call these tests the *synthetic force* experiments. In the second, we simulate satellites corotating with their orbital revolution, i.e. as if there were tidally locked. We call these the *rotating satellite* experiments.

The synthetic force experiments estimate satellite mass loss by adding known mass loss mechanisms to a non-orbiting satellite simulated in isolation. Satellite particles outside the tidal radius do not feel the satellite's gravity, allowing particles outside this radius to escape easily. As discussed in §2, we take x_e to be the tidal radius, not r_t. Satellite mass loss can drive structural evolution and change $\Phi_{sat}(r)$, hence we update x_e during the course of the simulations.

We present the results of our synthetic force experiments in Fig. 8. The curve labelled *Tidal* (long-dashed) in Fig.8 only includes tidal truncation and assumes $\alpha = 0$ in the tidal radius calculation (see §2 and Appendix A). We include the centrifugal force effect by including it when calculating x_e and we now set $\alpha = 0.75$ [3]. We include the Coriolis force by adding it to the force used to update each particle's velocity at every time step. The mass evolution of the resulting simulation is labelled *Tidal+Rotation* in Fig.8 (short-dashed) . Finally, we include resonant torques by adding angular momentum at the rate calculated from the numerical perturbation theory calculation plotted in Fig.7 between $T = 1.0$ and $T = 2.0$ according to each particle's energy and angular momentum. The curve labelled *Tidal+Rotation+Resonant torque* (dotted) includes all three mechanisms: tidal truncation, rotation (both the centrifugal and Coriolis effects), and the resonant torque.

We also plot the mass loss from the circular-orbit N-body simulation in Fig. 8 (solid line). The idealised simulation including all the processes matches the actual N-body simulation remarkably well. However, the choice of $\alpha = 0.75$, although quite reasonable, was rather arbitrary and we made this choice to match the circular orbit simulation. But Fig. 8 clearly shows that the resonant torque causes more than 70% of the satellite mass loss. The remaining 30% of the mass loss results from rotational effects. Tidal truncation does not cause much satellite mass loss.

A satellite whose frame corotates with its revolution on a circular orbit should not experience a resonant torque. So as a further test of the resonant torque mechanism, we compare the mass loss from a non-rotating satellite simulation to a rotating satellite simulation. The non-rotating satellite simulation is the same as in §3.1. For the rotating satellite simulation, the satellite particles are rotated every time step around an axis perpendicular to the orbital plane, which passes through the satellite's centre. They are rotated with the same frequency as the circular orbit frequency of the satellite in the host halo. This fixes the direction of the host halo centre in the satellite frame. Owing to this rotation, the halo does not feel a time-dependent external potential, and hence feels no resonant torque. The two simulations have the same initial conditions. However, owing to the artificial rotation, the rotating satellite feels an extra Coriolis force. During the course of rotating satellite simulation, we subtract this extra force to make the comparison more meaningful.

Fig. 9 shows that the rotating satellite loses only $\approx 40\%$ of the mass lost by the non-rotating satellite by $T = 5.0$. Moreover, the mass loss histories of both satellites are almost identical at early times ($T \leq 0.7$). This mass loss results from the adjustment of the satellite's initial conditions to the host halo potential. If we ignore satellite mass loss during this phase, the non-rotating satellite loses about five times more mass than the rotating satellite, again confirming that resonant torques are the dominant mechanism responsible for circular orbit satellite mass loss.

The mass loss rates in the *Tidal+Rotation* simulation in Fig. 8 and the *Rotating* satellite in Fig. 9 are almost identical if we ignore the early relaxation phase in the rotating satellite simulation. Both simulations attempt to reproduce

[3] Note that α is a free parameter and can be between 0 to 1.

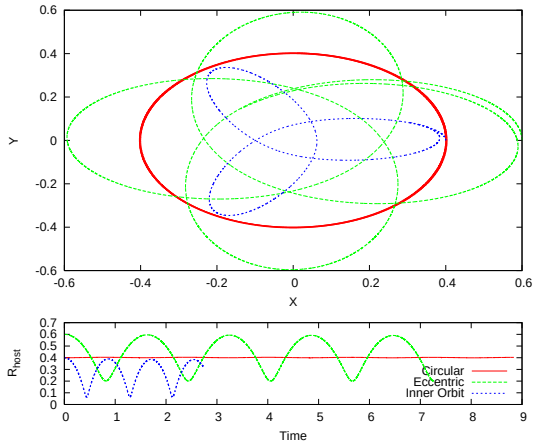

Figure 10. The circular, eccentric, and inner orbits. *Top panel:* the three trajectories in the orbital plane. *Bottom panel:* the time evolution of the distance between the satellite and the host halo centre.

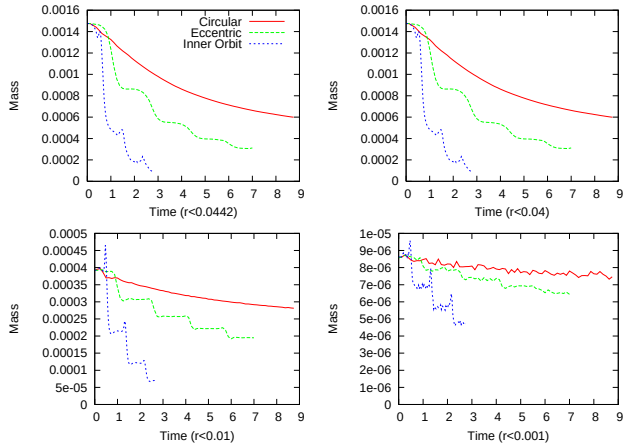

Figure 11. The mass evolution for the circular, eccentric, and inner orbit simulations. We plot the mass within radii of 0.045, 0.04, 0.01, and 0.001 versus time in the top left, top right, bottom left, and bottom right panels, respectively. The initial satellite radius is 0.045.

circular orbit satellite mass loss without resonant torque effects, using totally different approaches. This similarity confirms that our treatment for non-resonant mass loss captures the essential dynamics and implies that that our estimates of satellite mass loss in these experiments is reasonable. In conclusion, Figs. 8 and 9 confirm that resonant torque effects dominate circular orbit satellite mass loss.

4 SATELLITE DISRUPTION ON AN ECCENTRIC ORBIT

Several physical processes, including resonant torques, gravitational shocks with resonant shock effects, and continuous tidal truncation, simultaneously affect a satellite on an eccentric orbit. To study this complicated interplay and to understand the characteristics of the individual physical processes, we compare the evolution of three different simulations: a circular orbit simulation, an eccentric orbit simulation, and an inner orbit simulation (see Fig. 10). The circular orbit simulation is that described in §3. The eccentric orbit simulation is an $e = 0.5$ orbit with an apocentre of $r_{apo} = 0.6$ and a pericentre of $r_{peri} = 0.2$ [4]. The circular orbit and the eccentric orbit have the same orbital energy. The inner orbit simulation is an $e = 0.72$ orbit with an apocentre of $r_{apo} = 0.4$ and a pericentre of $r_{peri} = 0.064$. The normalised angular momentum (κ) of the inner orbit is 0.55, which is near the median κ of subhaloes in a sample taken from recent cosmological simulations (Ghigna et al. 1998; Zentner et al. 2005).

Fig. 11 shows the evolution of the enclosed mass within 90%, 22%, 2.2%, and 0.22% of the original satellite radius. The two eccentric orbit satellites lose their mass at pericentre episodically, while that for the circular orbit appears continuous. The eccentric-orbit satellites lose significantly more mass than the circular orbit satellite.

The computation of a satellite's gravitationally bound mass is difficult in practise and we use the mass enclosed within the truncation radius as a proxy. Fig. 12 shows the mass loss history for the three simulations using two different definitions of the bound satellite mass. The first definition is the total mass inside the initial satellite radius. The second definition is total mass inside the instantaneous tidal radius. We find that a satellite's mass rapidly decreases and then increases again around the time of pericentre passage, if we use the tidal radius definition for the bound mass. This mass evolution results from the rapid variation in the instantaneous tidal radius (Fig. 12, bottom). However, if this radius varies faster than the orbital time of an escaping particle, the tidal radius will not represent the dynamics of escape. Therefore, we generally use the initial satellite radius definition for our working definition of the bound satellite mass.

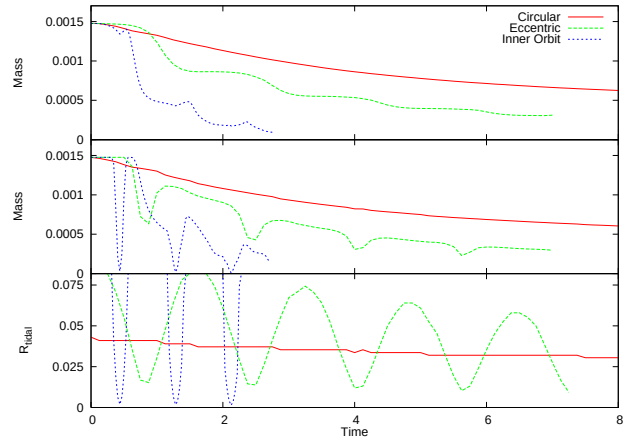

Figure 12. Evolution for the circular, eccentric and inner orbit simulations. *Top panel*: the mass enclosed within the initial satellite radius. *Middle panel*: the mass enclosed within the instantaneous tidal radius. *Bottom panel*: the evolution of the tidal radius.

[4] We define eccentricity as $e \equiv (r_{apo} - r_{peri})/(r_{apo} + r_{peri})$

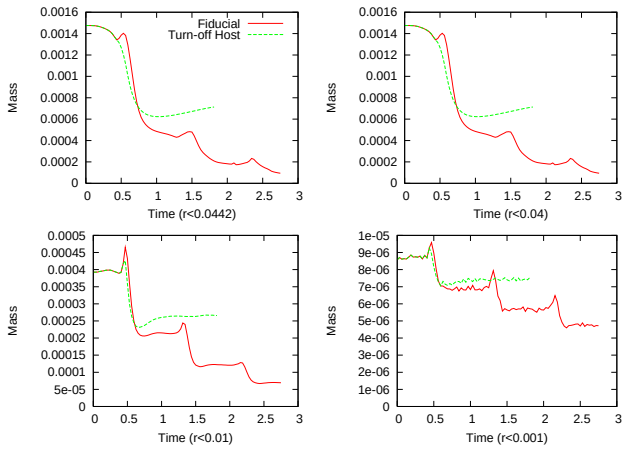

Figure 14. The figures show the enclosed mass evolution of two simulations: the fiducial simulation, which is the same as the inner orbit simulation, and the 'turn-off' host simulation, where the host halo potential is turned off at pericentre.

4.1 Heating by the gravitational shock at pericentre

According to Fig. 11, satellites on eccentric orbits lose mass mostly at pericentre. This suggests that satellite heating by the gravitational shock at pericentre is the dominant mechanism for satellite mass loss and disruption. We can discriminate two distinct effects of this gravitational shock: evolution of the satellite's structure and the persisting tidal truncation.

The top panel in Fig. 13 shows overlapping snapshots of the inner orbit simulation over one orbital period beginning from apocentre. The colour scale is logarithmic in satellite density. The lower-right panel shows the satellite evolution during pericentre passage. The satellite is compressed perpendicular to its trajectory and stretched out along its trajectory by the external potential. This deformation causes the density to increase, as observed in Fig. 11 where the enclosed mass within 90% (the top right panel), 22% (the bottom left panel), and 2.2% (the bottom right panel) of the original satellite radius increases at pericentre. The two bottom panels in Fig. 13 show blown-ups of the two boxed areas in the top panel. To highlight density differences, the colour now scales linearly with satellite density from $\rho = 1$ to $\rho = 100$, and white represents $\rho > 100$. The area of the white region in the right panel is larger than that of the left panel because of the density enhancement at pericentre.

The energy input from the gravitational shock reduces the satellite's binding energy, causing it to expand, and leads to tidal stripping. Work is done on the satellite potential to strip particles, this extra energy drives expansion and enhances the mass loss. In addition to enhancing the mass loss, the tidal truncation causes the satellite haloes to lose equilibrium. Fig. 12 shows that when the satellite moves deep inside the host halo, the tidal radius decreases. A large fraction of the satellite material outside of the tidal radius is not stripped and reenters the satellite when it again moves outward in the host halo and the tidal radius again increases. This rapidly changing tidal radius keeps the satellite haloes out of equilibrium.

To help understand the effect of the host halo potential, we compare two inner orbit simulations. The first simulation (fiducial) is the same as the original inner orbit simulation. The second simulation (turn-off host) is the same inner orbit simulation but we artificially "turn off" the host halo potential at pericentre ($T \approx 0.45$). We present the mass loss histories of these two simulations in Fig. 14. After turning off the host halo potential, the mass loss history of the two satellites diverges. The turn-off host simulation shows $\sim 15\%$ less mass loss than fiducial simulation. In addition, the satellite mass loss history of the turn-off host simulation shows an increase in mass after the significant mass loss caused by the gravitational shock, while the mass loss history of the fiducial simulation shows a continuous mass loss after the shock. The increase in mass results from lost particles returning to the satellite. Conversely, the persisting tidal truncation by the host halo potential in the fiducial simulation enhances satellite mass loss, causing the satellite halo to lose equilibrium and makes the evolution nonlinear.

In summary, both the internal structural evolution and the subsequent tidal truncation driven by time-dependent heating leads to significant evolution. These nonlinear physical processes are essential ingredients for an accurate prediction of satellite disruption and, therefore, simple approximations such as impulsive heating are insufficient (Spitzer 1987).

4.2 Resonant heating on an eccentric orbit satellite

We have divided the resonant dynamics of satellite evolution into a shock and a torque, but this distinction is arbitrary in principle. For example, both resonant effects simultaneously drive the evolution of a satellite on an eccentric orbit. A consistent perturbation theory calculation for an eccentric orbit perturber incorporates the full time dependence, coupling both the radial and the azimuthal orbital frequencies to a satellite's phase space. In addition, orbital decay adds the complication of a continuous spectrum of perturbation frequencies. Hence, a perturbation theory calculation for an eccentric orbit is a difficult and expensive. To get around this difficulty, we estimate the response by considering the most important frequencies one at a time. The strongest resonant effects are associated with the pericentric passage. We can, therefore, approximate the coupling with that of a circular satellite orbit at the pericentre radius and proceed as in §3.1.

Fig. 15 shows the locations of the resonances in satellite phase space for this equivalent circular orbit problem. We examined resonances with $l_1 \in [-10, 10]$ and $l \in [1, 4]$. In addition to the -1:2:2 resonance, the 0:1:1, 1:-1:1, and 1:0:2 resonances occur within the satellite's phase space. Comparing this to the results from the larger radius circular orbit calculation (§3.1), the coupling of the larger instantaneous angular frequency at pericentre to higher binding energy orbits that have larger orbital frequencies, moves the resonances inward in radius. Hence, some resonances that were previously outside the satellite in §3.1 are now within the satellite. In addition, the stronger tidal field at smaller orbital radii in the host increases the strength of the coupling. Using numerical perturbation theory, the strength of the 1:-1:1 and the 1:0:2 resonances are now comparable to

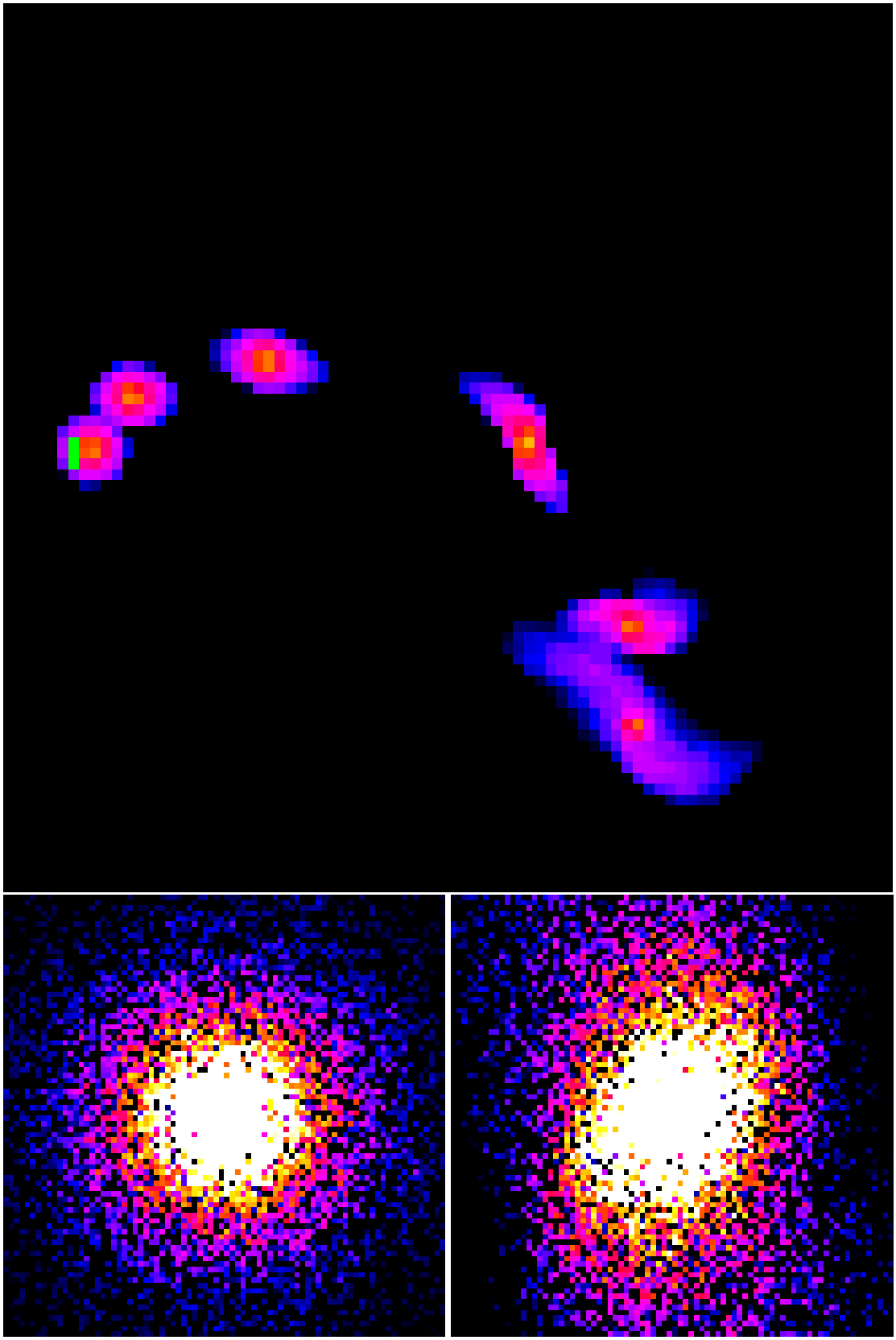

Figure 13. Snapshots of the inner orbit simulation for one radial period beginning at apocentre. *Top panel:* Overlapping snapshots of the satellite, shown at T =0.0, 0.16, 0.31, 0.47, 0.63, and 0.78. The origin of the inner axes (green) is the centre of the host halo. The dark matter density scales logarithmically with colour. *Bottom panels:* The satellites at $T = 0.0$ and $T = 0.31$ zoomed in to the size of the small boxes (green) in the top panel. To emphasise the dark matter density differences, the colour scale is now linear in density. The bottom snapshots show an increase in the size of the high density regions at $T = 0.31$ at pericentre compared to the satellite at $T = 0.0$ at apocentre.

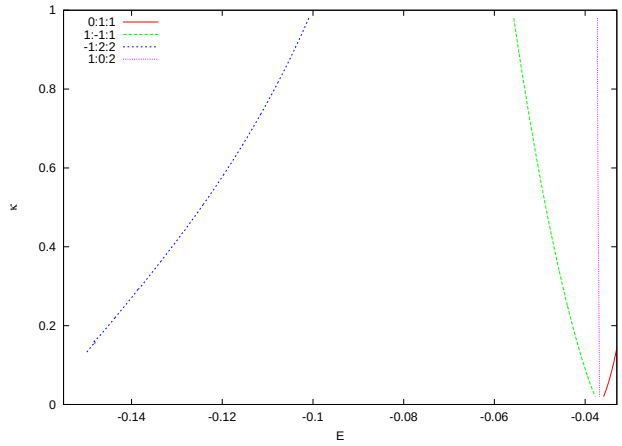

Figure 15. As in Fig. 4 but assuming a satellite frequency of $\Omega_{sat} = 6.56$, which corresponds to the frequency of a circular orbit at r_{peri} for the eccentric orbit simulation. Only the $l = 1$ and $l = 2$ resonances are shown. Unlike in Fig. 4, the 1:-1:1, 0:1:1, and 1:0:2 resonances are located inside the satellite.

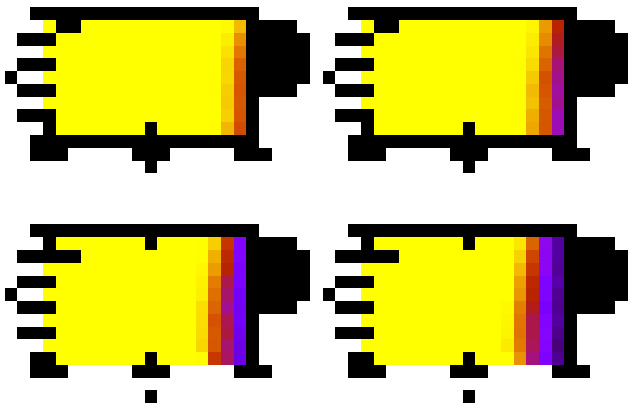

Figure 16. The fraction of particles remaining in phase space at different times. The colour code is linear from all particles stripped (0) to no particles stripped (1). Each panel shows the fraction of particles remaining at the labelled time compared to the initial satellite. Satellite stripping is an outside-in process in energy space.

the strength of the -1:2:2 resonance, which is much stronger than the -1:2:2 resonance in the larger radius circular orbit.

In summary, resonant heating is enhanced for an eccentric orbit both because of the larger number of resonances within the satellite and the stronger tidal force felt by the satellite at pericentre. However, our approximate perturbation theory calculation does not include the full time dependence of the eccentric orbit, a calculation that is extremely difficult and is beyond the scope of this paper.

5 SATELLITE STRIPPING AND ITS EFFECTS

5.1 The stripping process

Owing to satellite heating, particles in a satellite gain energy and angular momentum. This reduces the satellite's binding energy and enhances the satellite's mass loss. There are several mechanisms that heat a satellite and each one is effective over different ranges of binding energy. However, the re-equilibration of the satellite tends to globally redistribute the work throughout the satellite profile, washing out the nature of its origin. The observational signatures of the subsequent mass loss, then, tend to be universal.

Fig. 16 plots the fraction of bound particles remaining in different parts of phase space at different times for a satellite on a circular orbit. Low binding energy particles are stripped at earlier times and high binding energy particles are stripped later. In other words, the satellite stripping process is an outside-in process in energy space. We can understand this behaviour as follows. Weakly bound satellite orbits are affected and stripped by the tidal force beyond a characteristic radius. The apocentres of orbits with a given energy are within a factor of two of the radius of a circular orbit with the same energy, even for a zero-angular momentum orbit. For example, Fig. 17 marks the radius of a circular orbit ($\kappa = 1$) and the apocentre of a radial orbit ($\kappa = 0$) for an energy of $E = -0.044$; the apocentre of the radial orbit is only 50% larger than the radius of the circular orbit. Therefore, energy and not the relative angular momentum κ determines the stripping boundary. Although very low angular momentum orbits can be stripped at lower energies, Fig. 16 shows that any trend towards a larger escape fraction for smaller κ at fixed energy is very weak.

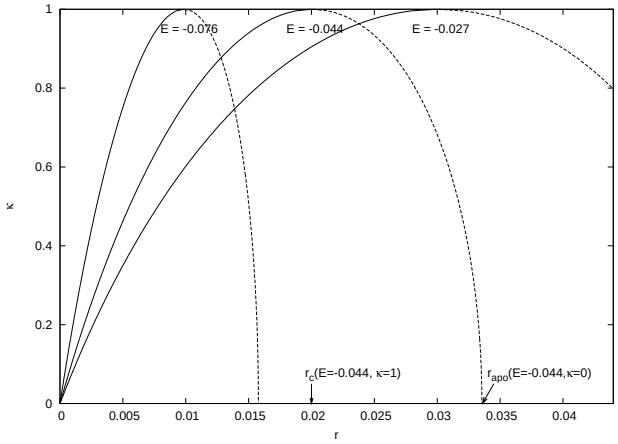

Figure 17. The apocentre and pericentre of orbits in the initial satellite model. Dashed lines represent the apocentre and solid lines the pericentre for orbits with energies of E =-0.076, -0.044, and -0.027. The radii for circular orbits with these energies are 0.01, 0.02, and 0.03, respectively. The x-axis is the distance from the halo centre and the y-axis is the normalised angular momentum, κ. The area between the pericentre and apocentre lines is the range in radii for orbits with each E and κ. The two arrows show the circular orbit radius and the apocentre radius for a radial orbit ($\kappa = 0$) with E =-0.044.

We plot the fraction of particles remaining in different parts of phase space for the eccentric orbit simulation in Fig. 18. The stripping process remains an outside-in process in energy space but now the trend toward a larger escape fraction at smaller relative angular momentum is stronger. This angular momentum dependence results from the time dependence of the tidal radius as shown in Fig. 12. Near a satellite's pericentre, satellite particles with low angular

Figure 18. The same as Fig. 16 but for the eccentric orbit simulation.

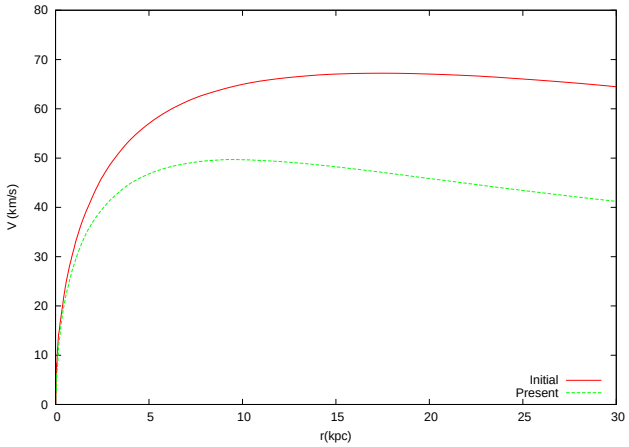

Figure 19. The circular velocity profile of the LMC dark matter halo at the initial and present time.

momentum are temporarily outside the instantaneous tidal radius and are prone to escape.

The outside-in stripping in energy space has interesting consequences for satellite evolution. Since the stars and cold gas in a satellite galaxy are centrally concentrated in their own dark matter halo, it protects them from stripping. The degree of *protection* for any component depends on its binding energy. For example, consider a disk and elliptical galaxy with the same linear extent[5] and the same orbit in the host halo. The disk galaxy contains material mostly on circular orbits, which have the largest binding energy at fixed radius, while the elliptical galaxy is made from a wide range of stellar orbits. We therefore predict that stars in the elliptical galaxy will be stripped sooner than stars in the disk galaxy. This difference should be incorporated into models of satellite galaxy stripping and when one estimates the subsequent stellar halo distribution.

5.2 The LMC stellar tail

The LMC is the largest Milky Way satellite. It has been the subject of numerous observational studies and characteristics of its structure and kinematics have been well established. However, the origin of the Magellanic Stream, a thin neutral hydrogen tail stretching over 100^o along a Galactic great circle, remains unexplained. Observations suggest that the Magellanic Stream may be a relic of a past interaction with the Milky Way (Mathewson et al. 1977; Putman et al. 1998). If this is the case, tidally stripped stellar ejecta should be observed as predicted by tidal interaction theory. However, none of the many searches for stellar ejecta has successfully detected a population of stars connected with the Magellanic Stream. Several scenarios have been suggested to resolve this conflict. First, the LMC gas may be removed by ram-pressure forces caused by an interaction with the outer disk (Moore & Davis 1994) or with hot gas in the Galactic halo (Mastropietro et al. 2005) instead of a tidal interaction. Second, the Stream may be a remnant from the tidal disruption of the Small Magellanic Cloud (SMC) owing to its gravitational interaction with the LMC and the Milky Way (Murai & Fujimoto 1980; Connors et al. 2006). Based on the results from the previous sections, we suggest that the LMC stars are protected by its dark matter halo while the Stream is the remnant of a low binding energy, extended neutral gas disk, analogous to the Milky Way's extended HI disk. Although smaller satellites and globular clusters have symmetric tidal tails, which has been used as an argument against a tidal origin for the Magellanic Stream (Moore & Davis 1994), larger satellites have a asymmetric tidal tails owing to the asymmetry in the tidal force (Choi et al. 2007). After the gas is stripped it would then hydrodynamically interact with the hot halo gas, changing the orbit of the gas in the stream (Mastropietro et al. 2005).

We implement an idealised simulation of LMC evolution in the Milky Way dark matter halo to test this hypothesis. The static Milky Way dark matter halo potential is based on the A1 model of Klypin et al. (2002); a $c = 12$ NFW halo with $R_{vir} = 258$ kpc, $M_{vir} = 1.0 \times 10^{12} M_{\odot}$, and $V_{max} = 163\,\mathrm{km/s}$. The live LMC halo model, which is also based on a $c = 12$ NFW halo model, is truncated at its x_e radius assuming that the LMC is located at $0.6R_{vir}$. To make a stable halo model we performed an Eddington inversion to the truncated LMC halo model, as presented in §2, and we realise a phase space of 10^6 equal-mass particles. The initial LMC halo circular velocity, $V_{max,LMC} = 0.42V_{max,host}$, is chosen to match the observed LMC circular velocity of $V_{max,LMC} = 0.3V_{max,host}$ (Kim et al. 1998; van der Marel et al. 2002) at the present day (see Fig. 19).

Since the LMC's evolutionary history is not well-defined, we assume a simple LMC orbit: an $e = 0.5$ orbit with a pericentre at $0.2R_{vir}$ and an apocentre at $0.6R_{vir}$. The current LMC is assumed to be located just after its pericentre (Gardiner et al. 1994; Gardiner & Noguchi 1996). The simulation starts at $0.6R_{vir}$ and runs a little more than two radial periods to represent the present-day LMC. It is worth noting that a consensus on the LMC orbital parameters has not yet been reached. Recent proper motion measurements using the Hubble Space Telescope (Kallivayalil et al. 2006) imply a very large galactocentric velocity. This large LMC velocity combined with an improved Milky Way mass model suggests either that the LMC

[5] In fact elliptical galaxies are generally more concentrated than disk galaxies.

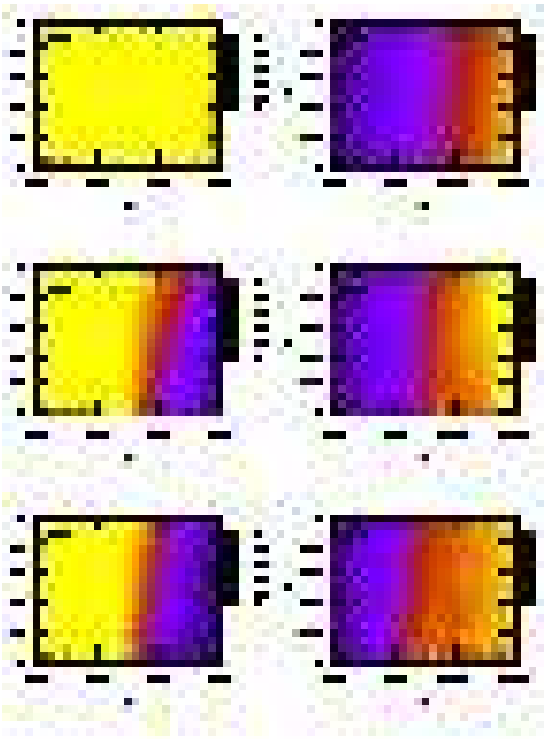

Figure 20. The distribution of particles remaining in the LMC halo at different times. *Left panels:* The fraction of particles remaining in the LMC halo based on their initial location in phase space (see Fig. 16). *Right panels:* The mean radius of the particles remaining as a function of phase space coordinates.

is on its first passage about the Milky Way or that its orbital period and apocentre must be a factor of 2 larger than previously estimated (Besla et al. 2007). In this paper, we take the classical LMC orbital parameters, which are based on the prescription induced by Murai & Fujimoto (1980). If it turns out that the classical point of view is false, our quantitative estimation should be revisited. However, our qualitative interpretation about the pattern of the LMC disruption is not sensitive to our particular choice of LMC orbital parameters.

Fig. 20 shows the fraction of particles remaining in the LMC in different parts of phase space (left panels) and their average distance from the LMC centre (right panels) at different times. Once again, the stripping corresponds to an outside-in process in energy space. Fig. 20 shows that particles with $E < -0.5$ have not yet been stripped. We assume that the LMC stars are mostly on circular orbits ($\kappa > 0.9$), because the visible LMC is a rotationally supported system. The current mean radius of the particles for $E = -0.5$ and $\kappa = 0.9$ is about 15 kpc, and hence LMC stars inside 15 kpc are expected to be protected by the dark matter halo, which is larger than the observed disk radius of 10 kpc (Kunkel et al. 1997). This suggests that the detectable signature of the LMC stellar ejecta could be very small.

5.3 Density profiles and rotation curves

The left panels in Fig. 21 show the evolution of the density profiles for the three different orbit simulations. As expected given the mass loss rates shown in Fig. 11, the inner orbit satellite's density profile evolves the most and the circular orbit's density profile evolves the least. However, even though the mass loss rates are different, the overall trends in the density profile evolution for the three satellites are similar. A decrease in density occurs at all radii, which is particularly evident in the inner orbit simulation, where even at $r \leq 0.001$ the density decreases uniformly with time. Although the density decreases, the steepness of the density profile does not decrease. Hence, the inner cusp is preserved during tidal mass loss, i.e. the evolution of satellites owing to interactions with their host halo will not remove NFW central cusps to make them agree more with observed density profiles (Diemand et al. 2007; Springel et al. 2008).

One can see the effect on the circular velocity profiles for the satellites on the three different orbits in the right panels of Fig. 21. Once again, even though the peak circular velocity drops from, the shape of the circular velocity profile does not change dramatically. In particular, the central circular velocity profile is still steeply rising. Stoehr (2006) claim that the circular velocity profiles of subhaloes are best fit by a parabolic function, which is shallower than NFW circular velocity profiles, and that this confirms their earlier result that the internal structure and kinematics of the Milky Way satellites are in good agreement with the subhaloes found in CDM simulations (Stoehr et al. 2002). The persistence of the steep inner density structure in our satellite simulations conflicts with their assumed parabolic velocity profile. Recent very high resolution simulations following the formation of CDM haloes in a cosmological context also have steep central density profiles in their subhaloes, which confirms our result (Diemand et al. 2008; Springel et al. 2008).

6 ESTIMATING SATELLITE MASS LOSS

To estimate satellite mass loss, researchers often use the impulse approximation. The impulse approximation assumes that the perturbation time scale is much shorter than the internal dynamical time scale (Spitzer 1987). However, in §3 and §4, we demonstrated that satellite halo evolution results from resonant effects, internal structure evolution, and tidal truncation in addition to impulses. In this section we will include the two resonant effects described in §3 to produce an improved analytic estimate. We implement these approximations in a simple model that computes the mass loss by tidal truncation, gravitational shocks, and resonant torques in spherical shells. For the tests presented here, we use the same satellite models and orbits presented in §§2–4. At each time step, we proceed as follows:

(i) The tidal radius x_e is computed for the current position in the satellite's orbit. The instantaneous satellite mass is the mass of all particles with $r < x_e$ and the remainder is considered to be stripped.

(ii) The satellite's mass *outside* of the tidal radius is gradually stripped on a crossing time scale. In particular, for each time step we remove a mass fraction of $\Delta t/t_{orb}$, where t_{orb} is the orbital period at the half mass radius of the satellite.

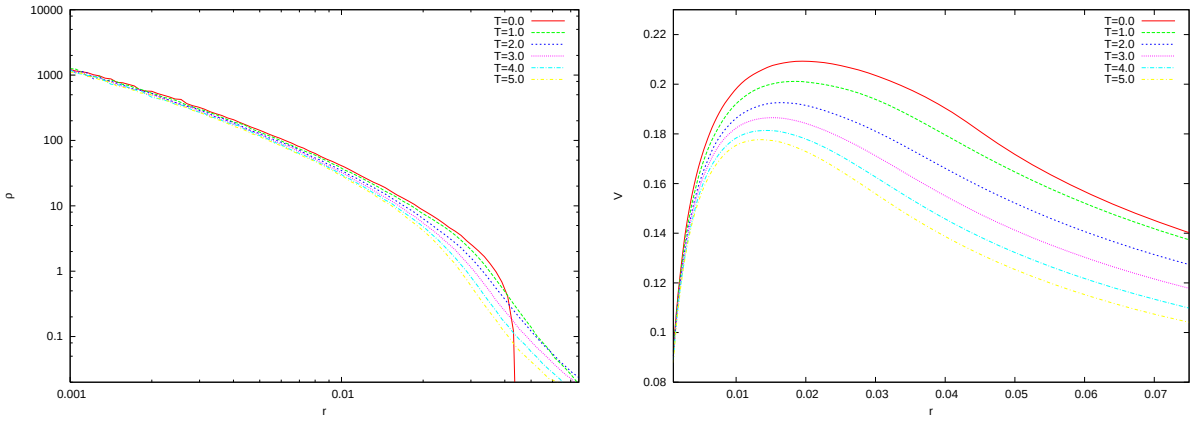

(a) The circular orbit

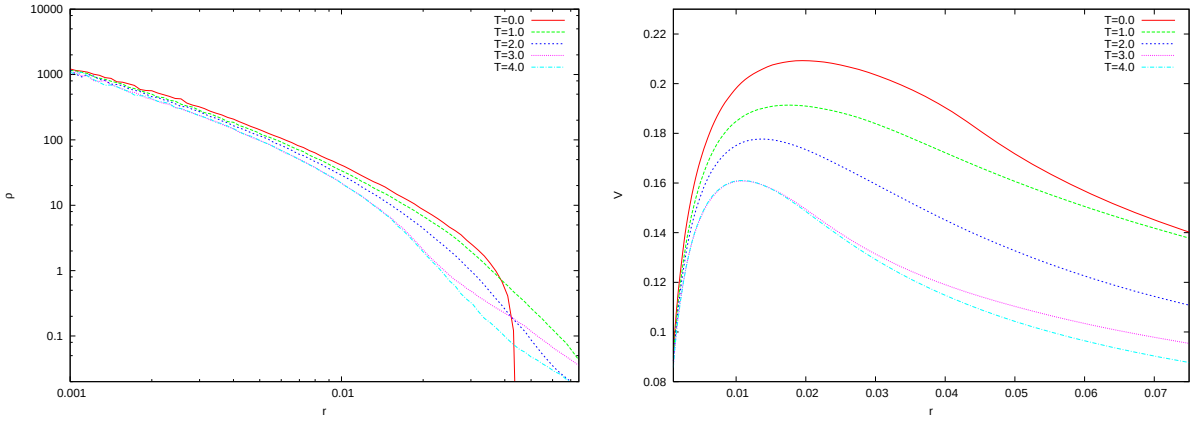

(b) The eccentric orbit

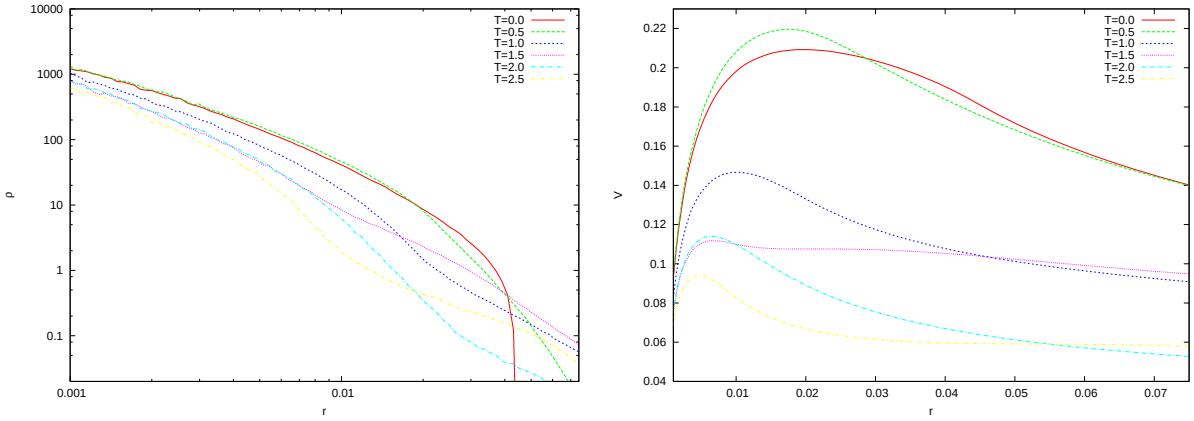

(c) The inner orbit

Figure 21. The density profiles (left panels) and rotation curves (right panels) of the satellite dark matter haloes for the three satellite orbit simulations at various times.

This procedure prevents unrealistic immediate and permanent satellite mass stripping outside the tidal radius (see §4.1).

(iii) The changes in energy and angular momentum for a given mass shell caused by the time-dependent external potential are computed in two parts: 1) the change in energy from gravitational shocks is only computed at every pericentre; and 2) the change in angular momentum owing to the resonant torque is computed at every step.

(iv) An increase in energy and angular momentum generally results in reducing the density of a mass shell. Overall, the reduction in density results in mass loss, decreases x_e, and hence drives further mass loss.

This mass loss algorithm is similar to the scheme used in Taylor & Babul (2001, 2004, 2005a,b). It provides the satellite mass loss history, which can be used to compare with the simulation results.

We determine the tidal radius as the satellite radius where $d\Phi_{eff} = 0$ (see §2 and Appendix A). Since this model

does not include any velocity information about individual satellite particles, our estimate cannot include the Coriolis force. Instead we choose $\alpha = 1.0$ when evaluating Φ_{eff} to compensate for ignoring the Coriolis force.

For the gravitational shock heating, we compute the change in energy using the impulse approximation with an adiabatic correction. Assuming an spherical isothermal host halo, Gnedin et al. (1999) derive the following expression for the energy change:

$$\Delta E = \frac{1}{6}\left(\frac{\pi r}{R_p^2 V_p}\right)^2 \frac{M_{halo}}{R_p} A(x) \quad (2)$$

where r is the satellite's radius, R_p is the pericentre distance, and V_p is the satellite's velocity at pericentre. M_{halo} is the mass of the perturber, which for us is the enclosed halo mass at pericentre. The quantity $A(x)$, the *adiabatic* correction, reduces the heating if the internal orbital time is significantly shorter than the impulsive time scale. We explore both the Spitzer correction and the Weinberg correction (Weinberg 1994a,b; Gnedin & Ostriker 1999):

$$A(x) = \exp(-2x^2) \quad \text{(Spitzer)} \quad (3)$$

$$A(x) = (1+x)^{-1.5} \quad \text{(Weinberg)} \quad (4)$$

where $x = \omega\pi R_p/V_p$ and ω is the azimuthal frequency of an orbit at r. Equations (2)–(4) determine the energy change for each mass shell and for each shock event. The added energy expands the satellite. Using the virial theorem, the expansion rate can be estimated as $\Delta r = \Delta E r^2$ (Taylor & Babul 2001). This satellite expansion reduces the density in each shell: $\Delta\rho = -(9/2\pi)(\Delta E/r^2)$. We use this relationship to compute the mass loss in Step (iv) of the algorithm above.

In addition to heating by gravitational shocks, the results from §3 confirm that heating by resonant torques plays an important role in satellite mass loss. This effect has not been included in most studies of satellite evolution. To accurately estimate the resonant torque, one needs high quality N-body simulations (see Weinberg & Katz 2007a) or perturbation theory calculations (Weinberg 1986, 1989). However, we can estimate the torque using a simple model as follows. First, we compute the torque on a mass shell by assigning the mass in the shell to an equivalent ring. The torque on the ring is computed using a simple spin-orbit coupling calculation as in a planet–satellite interaction. In this approximation, we assume that the host halo potential is a point mass at the centre of the host halo. We model the quadruple moment of a satellite mass shell as two equal, diametrically opposed point masses in the satellite's orbital plane, separated by the diameter of the mass shell. Owing to the separation, the gravitational forces on the two masses differ. The differential gravitational force torques the two masses and we evaluate the total torque on the satellite's mass shell by integrating this torque through the ring.

The mathematical form of the torque on the mass shell is then

$$\tau_{ring}(R) = 6GM\frac{R}{R_{sat}} \quad (5)$$

where R_{sat} is the distance from the host halo centre to the satellite, R is the distance from the satellite centre to a given mass shell, and M is the enclosed host halo mass (Murray & Dermott 1999, Chapter 5.3 see their Fig. 5.7).

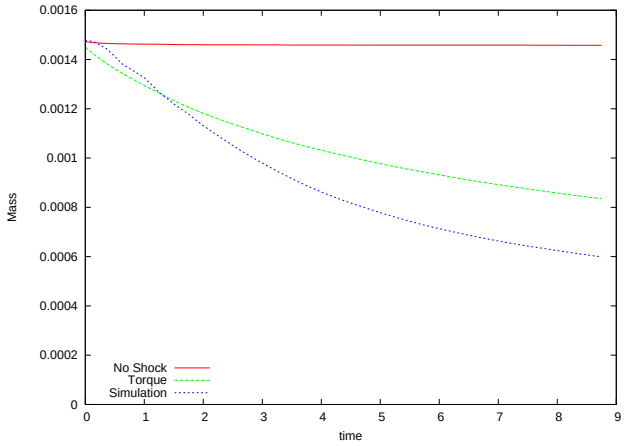

Figure 22. The mass loss history of the circular orbit simulation. Analytic estimates of the mass loss history are compared with the simulation. *No Shock* is an analytic estimate only including tidal truncation and *Torque* is an analytic estimate including the effects of tidal truncation and resonant torques.

Equation (5) provides the specific torque on the satellite mass shell.

Second, we compute the fraction of resonant orbits in each mass shell. Equation (5) computes the torque on a rigid mass shell, not the torque on the mass shell owing to the resonant interaction. To estimate the resonant torque, we estimate the mass fraction of resonantly coupled orbits in the mass shell and multiply the torque on the rigid mass shell by this fraction. As shown in equation (1), determining resonant orbits requires detailed calculations. Using equation (24) of Weinberg (1994b), Gnedin & Ostriker (1999) show that the number of stars at the peak amplitude scales as $1/\tau$, where τ is the characteristic duration of the shock. The resonant shock and the resonant torque are based on the same physics with a different coupling and frequency. By dimensional analysis, $1/\tau \sim \omega$, where ω is the angular frequency of satellite mass shell [6]. Therefore, we estimate this fraction as the ratio of the azimuthal angular frequency of the orbiting satellite to the angular frequency of the satellite's mass shell. Consequently, the torque on the satellite mass shell becomes:

$$\tau_{sat}(R) = \tau_{ring}(R) \times \begin{cases} \left(\frac{\Omega_s}{\omega(R)}\right) & \text{if } \Omega_s \le \omega(R) \\ \left(\frac{\omega(R)}{\Omega_s}\right) & \text{if } \Omega_s > \omega(R) \end{cases} \quad (6)$$

This torque leads to expansion and the expansion rate can be estimated as

$$\Delta r = \sqrt{\frac{4r}{M_{sat}(r)}}\tau_{sat}\Delta t. \quad (7)$$

This expansion reduces the satellite's density as $\Delta\rho \propto -\frac{\Delta r}{r^4}$. We also use this relationship to compute the mass loss in Step (iv) of the algorithm above.

[6] The angular frequency $\omega = \frac{V_c}{R}$ where V_c is the circular velocity and R is the radius of a given mass shell.

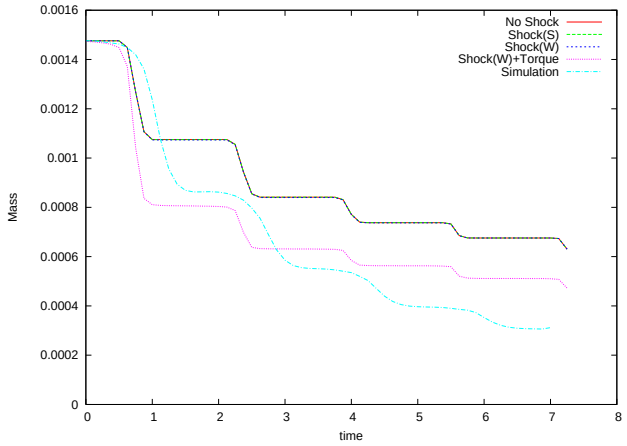

Figure 23. The mass loss history for the eccentric orbit simulation. Analytic estimates of the mass loss history are compared with the simulation results. *No Shock* is an analytic estimate only including tidal truncation. *Shock(S)* is an analytic estimate including tidal truncation and impulse shock heating with the Spitzer correction. *Shock(W)* is an analytic estimation including the effects of tidal truncation and impulse shock heating with the Weinberg correction. *Shock(W) + Torque* is the same as *Shock(W)* but with the addition of the resonant torque.

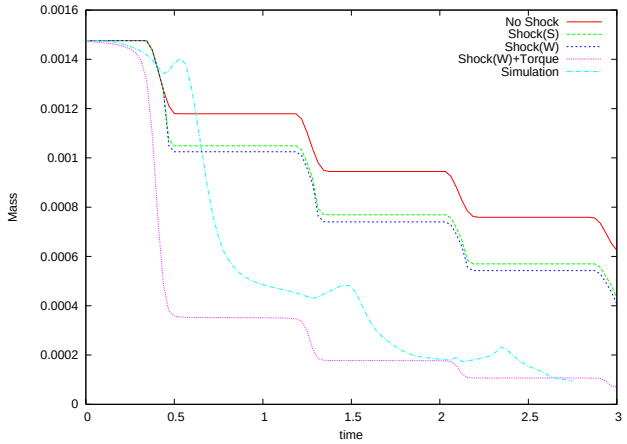

Figure 24. The same as Fig. 23 but for the inner orbit simulation.

The mass loss histories for the circular orbit simulation, the eccentric orbit simulation, and the inner orbit simulation are compared with the results of our mass-loss algorithm in Figs. 22 – 24, respectively. For the circular orbit case, there are no gravitational shocks. Fig. 22 shows two analytic estimates: *No Shock* and *Torque*. The *No Shock* estimate only includes tidal truncation and predicts negligible mass loss. The *Torque* estimate includes both the resonant torque approximation and tidal truncation. Its mass loss history is much more similar to the simulation: more than 50% of the original mass is lost. This suggests that mass loss for a satellite on a circular orbit mainly results from resonant torques and our algorithm for resonant torque provides a dramatically improved description.

For the eccentric orbit and inner orbit simulation cases, the gravitational shock plays an important role in driving mass loss. Figs. 23 and 24 compares our mass loss algorithm to the simulations. Here, we include the *No Shock* model, the impulse approximation with the Spitzer correction [*Shock(S)*], the impulse approximation with the Weinberg correction [*Shock(W)*], and the impulse approximation with Weinberg correction together with our resonant torque approximation [*Shock(W)+Torque*]. All the estimates include tidal truncation. The *Shock(W)+Torque* model best represents the mass loss seen in the simulation while the *Shock(W)* with no resonant torque predicts less mass loss than that seen. The importance of the resonant torque is most obvious for the inner orbit simulation. Compared to the simulation, the estimate including the shock and the resonant torque [*Shock(W)+Torque*] does significantly better estimating the mass loss in the simulation than that of the shock alone, which significantly underpredicts the mass loss. Tidal truncation alone [*No Shock*] shows the worst agreement.

Although our new algorithm provides a dramatically improved satellite mass loss history, discrepancies remain owing to the many complicated physical processes involved in satellite disruption. First, the compressive gravitational shock is a strongly non-linear, time-dependent perturbation. Although the adiabatic correction includes some of this time dependence by including the work done at the frequency peak, many channels of possible coupling are ignored. Second, satellite heating by resonant interactions is too complicated to be accurately represented by our simple parametrisation. For example, the adiabatic correction extends the coupling to lower energies by noting that the resonant coupling will have a power law rather than an exponential scaling with frequency. However, for a particular interaction, individual resonances may dominate the response; this is analogous to the difference between a *line* and *continuous* spectrum. Third, a real satellite halo has a wide range of orbits, from circular to radial. The mass shell scheme cannot accurately capture the dynamics of these different orbits. Moreover, the entire satellite structure readjusts its evolution in the course of satellite disruption. This readjustment process is also not included. These arguments suggest that although our new algorithm provides improved satellite mass loss histories, high quality simulations are still necessary for an accurate prediction of mass loss.

7 SUMMARY AND CONCLUSIONS

Using high resolution simulations with cosmologically motivated initial conditions, we investigate the physical processes responsible for the evolution of satellite galaxies in their host halo. We identified and explored the following important physical mechanisms that result in satellite galaxy disruption. Our main results are as follows:

(i) Resonant mechanisms of two types play a key role in satellite disruption: the resonant shock and the resonant torque.

(ii) We studied satellites on circular orbits to isolate the effects of resonant torques. The ILR-like resonance $l_1 : l_2 : l_3 = -1 : 2 : 2$ (see equation (1)) dominates the torque resonance because all the $l = 1$ resonances and the 0:2:2 (corotation-like) and the 1:2:2 (OLR-like) resonances are located outside the satellite's tidal radius.

(iii) Some important resonances require more particles than are typically used in cosmological simulations. For example, to accurately reproduce the heating from the -1:2:2 resonance, a satellite simulation needs more than 10^5 particles within the virial radius for our expansion code and possibly more for codes affected by small-scale noise, e.g. a tree code. Too few particles results in less mass loss and it suggests that the lifetime of dark matter subhaloes in current cosmological simulations could be *overestimated*.

(iv) For satellites on eccentric orbits, gravitational shocks dominate the heating but the heating rate is significantly underestimated by the impulse approximation for several reasons. First, strong low-order resonances couple to the phase space in the 'adiabatic' regime and the work done on the satellite drives structural evolution. Second, the ongoing tidal truncation affects the dynamics of the escaping material and the satellite's size. The interplay of these mechanisms leads to continuous mass loss and evolution.

(v) The number of resonances in a satellite increases as the satellite's orbital frequency increases; the strength of each resonant interaction also increases. This affects satellites on low-energy and low-angular momentum orbits which have small pericentres and high satellite azimuthal frequencies.

(vi) Satellite mass stripping is an outside-in process in energy space. We discuss the morphological consequences for the stripping signatures of stellar and gaseous streams.

(vii) We present an improved algorithm to estimate satellite mass loss including both resonant shocks and torques. We show that the mass-loss history computed using this algorithm reproduces the general features seen in the simulations.

The satellite evolution using N-body simulation has been studied by a number of authors recently (e.g. Hayashi et al. 2003; Kazantzidis et al. 2004; Boylan-Kolchin & Ma 2007). Their approach differs ours in several ways. We use a highly idealised simulation configuration to better discern the details of the dynamical mechanisms, focussing on the detailed physical processes affecting satellite evolution such as resonant dynamics that have not been rigorously addressed elsewhere. For example, we equilibrated the initially tidally truncated satellite to reduce the artificial perturbation from sudden introduction of the host halo potential. We also explored a circular orbit simulation to clearly demonstrate the effects of resonant torque. We performed a linear perturbation calculation to estimate the required resolution for resonant effect, and made the simulations satisfy this requirement. In addition, we use an expansion code to reduce the force fluctuations on small scales. Owing to these efforts, we were able to demonstrate the importance of the resonant torque in satellite disruption.

Hayashi et al. (2003) used an NFW halo as a satellite initial conditions and a Tree code for a potential solver. They found that the simple tidal-limit approximation underestimates the mass loss, as we do, and found structural evolution, also similar to our findings. Kazantzidis et al. (2004) and Boylan-Kolchin & Ma (2007) also found that similar internal structure evolution using tree-code simulations. This consensus suggests that the inner cusp of satellite halo is not strongly affected by the tides from the host halo. However, owing to their rather complicated configuration, they could not discern the effect of the resonant torque, although some authors (e.g. Hayashi et al. 2003) has noticed that analytic formulae underestimate the mass loss.

Although we have improved our understanding of the detailed physical processes responsible for satellite disruption, some issues remain. By separating the heating mechanisms into two distinct regimes, we achieved an improved understanding of resonant dynamics for an eccentric orbit. However, we have not compared this approximation with a comprehensive perturbation theory calculation. The resonant heating of satellites on eccentric orbits is similar to heating by other subhaloes. This interaction is an important source of satellite evolution in addition to the interaction with the smooth host halo. In addition, the initially spherical satellite is deformed during disruption owing to the host halo's tidal field and we have not yet accounted for this deformation. A comprehensive treatment of this deformation might be necessary to understand satellite disruption in detail. Lastly, we also need a better understanding of the non-linear processes that occur during satellite evolution.

In this study, we characterised the linear processes; understanding the detailed consequences of the non-linear processes is a daunting future task. We should then finally be able to fully constrain the satellite disruption mechanism, which is an essential ingredient of galaxy formation and evolution.

ACKNOWLEDGMENTS

This work was supported in part by NASA awards ATP NAGS-13308 and NAG5-12038.

APPENDIX A: A SATELLITE'S EFFECTIVE POTENTIAL IN A GENERAL GRAVITATIONAL FIELD AND A UNIFORMLY ROTATING FRAME

The effective potential of a spherical satellite as function of a satellite's radius ($\boldsymbol{r}$) is determined by its self-gravity, the external potential, and the centrifugal force. We set $\boldsymbol{r} = \boldsymbol{R} - \boldsymbol{R_0}$ where $\boldsymbol{R}$ is the location relative to the host halo's centre and $\boldsymbol{R_0}$ is the location of the satellite's centre relative to the host halo's centre. The acceleration in the satellite's frame, $\ddot{\boldsymbol{r}}$, is difference between the acceleration, $\ddot{\boldsymbol{R}}$, and the effective acceleration of the satellite, $\ddot{\boldsymbol{R}}_{\boldsymbol{0}}$, in the host frame. The quantities $\ddot{\boldsymbol{R}}$ and $\ddot{\boldsymbol{R}}_{\boldsymbol{0}}$ are

$$\ddot{\boldsymbol{R}} = -\nabla\Phi_{tot}(\boldsymbol{R}) - \boldsymbol{\Omega}\times(\boldsymbol{\Omega}\times\boldsymbol{R}), \quad \text{(A1)}$$

$$\ddot{\boldsymbol{R}}_{\boldsymbol{0}} = -\nabla\Phi_{tot}(\boldsymbol{R_0}) - \boldsymbol{\Omega}\times(\boldsymbol{\Omega}\times\boldsymbol{R_0}), \quad \text{(A2)}$$

where $\Phi_{tot}(\boldsymbol{R})$ is the total potential on the particle and $\boldsymbol{\Omega}$ is angular velocity of the satellite. The quantity $\Phi_{tot}(\boldsymbol{R}) = \Phi_{host}(\boldsymbol{R}) + \Phi_{sat}(\boldsymbol{R})$, where $\Phi_{host}(\boldsymbol{R})$ is the host halo potential and $\Phi_{sat}(\boldsymbol{R})$ is the potential of the satellite. Using $\ddot{\boldsymbol{r}} = \ddot{\boldsymbol{R}} - \ddot{\boldsymbol{R}}_{\boldsymbol{0}}$, the equation of motion in the satellite frame becomes

$$\ddot{\boldsymbol{r}} = -\nabla\Phi_{sat}(\boldsymbol{r}) - \nabla\Phi_{host}(\boldsymbol{R}) - \nabla\Phi_{host}(\boldsymbol{R_0}) - \boldsymbol{\Omega}\times(\boldsymbol{\Omega}\times\boldsymbol{r}). \quad \text{(A3)}$$

Because we assume a circular orbit, $\Phi_{sat}(\boldsymbol{R_0})$ is a

constant; $\nabla\Phi_{sat}(\boldsymbol{R}) \rightarrow \nabla\Phi_{sat}(\boldsymbol{r})$ and $\nabla\Phi_{tot}(\boldsymbol{R_0}) \rightarrow \nabla\Phi_{host}(\boldsymbol{R_0})$. The second and third terms in equation (A3) can be further simplified using a Taylor expansion,

$$\begin{aligned} - \quad & \nabla\Phi_{host}(\boldsymbol{R}) - \nabla\Phi_{host}(\boldsymbol{R_0}) = \\ - \quad & \frac{d^2\Phi_{host}(\boldsymbol{R_0})}{dR^2}\boldsymbol{r} + \mathcal{O}\left[(r/R_o)^2\right]. \end{aligned} \tag{A4}$$

The last term in equation (A3) is the centrifugal term. Assuming that the orbital plane is equatorial with $\hat{\Omega} = \hat{z}$ and $\boldsymbol{r} = (x, y, x)$, we have

$$-\boldsymbol{\Omega} \times (\boldsymbol{\Omega} \times \boldsymbol{r}) = -[(\boldsymbol{\Omega} \cdot \boldsymbol{r})\boldsymbol{\Omega} - (\boldsymbol{\Omega} \cdot \boldsymbol{\Omega})\boldsymbol{r}] = \Omega^2(x, y, 0). \tag{A5}$$

For generating initial conditions in §2 and our idealised models in §6, we will approximate equation (A5) with a spherical average

$$-\boldsymbol{\Omega} \times (\boldsymbol{\Omega} \times \boldsymbol{r}) \approx \alpha\Omega^2\boldsymbol{r} \tag{A6}$$

where α is between 0 and 1.

Using this expansion, equation (A3) becomes

$$\begin{aligned} \ddot{\boldsymbol{r}} \quad &= \quad -\nabla\Phi_{sat}(\boldsymbol{r}) - \frac{d^2\Phi_{host}(\boldsymbol{R_0})}{dR^2}\boldsymbol{r} + \alpha\Omega^2\boldsymbol{r} \\ &= \quad -\nabla\Phi_{sat}(\boldsymbol{r}) - [4\pi G\rho_{host}(R_0) - (2+\alpha)\Omega^2]\boldsymbol{r}. \end{aligned} \tag{A7}$$

Finally, a satellite's effective potential as function of $\boldsymbol{r}$ using equation (A7) can be written as:

$$\begin{aligned} \Phi_{eff}(\boldsymbol{r}) \quad &= \quad \Phi_{sat}(\boldsymbol{r}) \\ &+ \quad \left[4\pi G\rho_{host}(\boldsymbol{R_0}) - (2+\alpha)\Omega^2\right] \times \left(\frac{1}{2}r^2\right). \end{aligned} \tag{A8}$$

REFERENCES

Besla G., Kallivayalil N., Hernquist L., Robertson B., Cox T. J., van der Marel R. P., Alcock C., 2007, ApJ, 668, 949

Binney J., Tremaine S., 1987, Galactic dynamics. Princeton, NJ, Princeton University Press, 1987

Boylan-Kolchin M., Ma C.-P., 2007, MNRAS, 374, 1227

Bullock J. S., Kravtsov A. V., Weinberg D. H., 2001, ApJ, 548, 33

Chernoff D. F., Weinberg M. D., 1990, ApJ, 351, 121

Choi J.-H., Weinberg M. D., Katz N., 2007, MNRAS, 381, 987

Clutton-Brock M., 1972, Ap&SS, 16, 101

Clutton-Brock M., 1973, Ap&SS, 23, 55

Connors T. W., Kawata D., Gibson B. K., 2006, MNRAS, 371, 108

De Lucia G., Kauffmann G., Springel V., White S. D. M., Lanzoni B., Stoehr F., Tormen G., Yoshida N., 2004, MNRAS, 348, 333

Diemand J., Kuhlen M., Madau P., 2007, ApJ, 667, 859

Diemand J., Kuhlen M., Madau P., Zemp M., Moore B., Potter D., Stadel J., 2008, Nature, 454, 735

Diemand J., Moore B., Stadel J., 2004, MNRAS, 352, 535

Gao L., White S. D. M., Jenkins A., Stoehr F., Springel V., 2004, MNRAS, 355, 819

Gardiner L. T., Noguchi M., 1996, MNRAS, 278, 191

Gardiner L. T., Sawa T., Fujimoto M., 1994, MNRAS, 266, 567

Ghigna S., Moore B., Governato F., Lake G., Quinn T., Stadel J., 1998, MNRAS, 300, 146

Ghigna S., Moore B., Governato F., Lake G., Quinn T., Stadel J., 2000, ApJ, 544, 616

Gnedin O. Y., Hernquist L., Ostriker J. P., 1999, ApJ, 514, 109

Gnedin O. Y., Ostriker J. P., 1999, ApJ, 513, 626

Hayashi E., Navarro J. F., Taylor J. E., Stadel J., Quinn T., 2003, ApJ, 584, 541

Hernquist L., Ostriker J. P., 1992, ApJ, 386, 375

Kallivayalil N., van der Marel R. P., Alcock C., Axelrod T., Cook K. H., Drake A. J., Geha M., 2006, ApJ, 638, 772

Kazantzidis S., Mayer L., Mastropietro C., Diemand J., Stadel J., Moore B., 2004, ApJ, 608, 663

Kim S., Staveley-Smith L., Dopita M. A., Freeman K. C., Sault R. J., Kesteven M. J., McConnell D., 1998, ApJ, 503, 674

Klypin A., Gottlöber S., Kravtsov A. V., Khokhlov A. M., 1999, ApJ, 516, 530

Klypin A., Zhao H., Somerville R. S., 2002, ApJ, 573, 597

Kunkel W. E., Demers S., Irwin M. J., Albert L., 1997, ApJL, 488, L129+

Majewski S. R. et al., AJ, 128, 245

Mastropietro C., Moore B., Mayer L., Wadsley J., Stadel J., 2005, MNRAS, 363, 509

Mathewson D. S., Schwarz M. P., Murray J. D., 1977, ApJL, 217, L5

Moore B., Davis M., 1994, MNRAS, 270, 209

Moore B., Katz N., Lake G., 1996, ApJ, 457, 455

Murai T., Fujimoto M., 1980, PASJ, 32, 581

Murali C., Katz N., Hernquist L., Weinberg D. H., Davé R., 2002, ApJ, 571, 1

Murray C. D., Dermott S. F., 1999, Solar system dynamics. Solar system dynamics by Murray, C. D., 1999

Navarro J. F., Frenk C. S., White S. D. M., 1997, ApJ, 490, 493

Oguri M., Lee J., 2004, MNRAS, 355, 120

Peñarrubia J., Navarro J. F., McConnachie A. W., 2008, ApJ, 673, 226

Putman M. E. et al. 1998, Nature, 394, 752

Quilis V., Moore B., Bower R., 2000, Science, 288, 1617

Read J. I., Wilkinson M. I., Evans N. W., Gilmore G., Kleyna J. T., 2006, MNRAS, 367, 387

Spitzer L., 1987, Dynamical evolution of globular clusters. Princeton, NJ, Princeton University Press, 1987

Springel V., Wang J., Vogelsberger M., Ludlow A., Jenkins A., Helmi A., Navarro J. F., Frenk C. S., White S. D. M., 2008, MNRAS, 391, 1685

Stoehr F., 2006, MNRAS, 365, 147

Stoehr F., White S. D. M., Tormen G., Springel V., 2002, MNRAS, 335, L84

Taylor J. E., Babul A., 2001, ApJ, 559, 716

Taylor J. E., Babul A., 2004, MNRAS, 348, 811

Taylor J. E., Babul A., 2005a, MNRAS, 364, 515

Taylor J. E., Babul A., 2005b, MNRAS, 364, 535

Tremaine S., Weinberg M. D., 1984, MNRAS, 209, 729

van der Marel R. P., Alves D. R., Hardy E., Suntzeff N. B., 2002, AJ, 124, 2639

Weinberg M. D., 1986, ApJ, 300, 93

Weinberg M. D., 1989, MNRAS, 239, 549

Weinberg M. D., 1994a, AJ, 108, 1398

Weinberg M. D., 1994b, AJ, 108, 1403

Weinberg M. D., 1999, AJ, 117, 629

Weinberg M. D., 2004, astro-ph/0404169

Weinberg M. D., Katz N., 2007a, MNRAS, 375, 425
Weinberg M. D., Katz N., 2007b, MNRAS, 375, 460
Zentner A. R., Berlind A. A., Bullock J. S., Kravtsov A. V., Wechsler R. H., 2005, ApJ, 624, 505

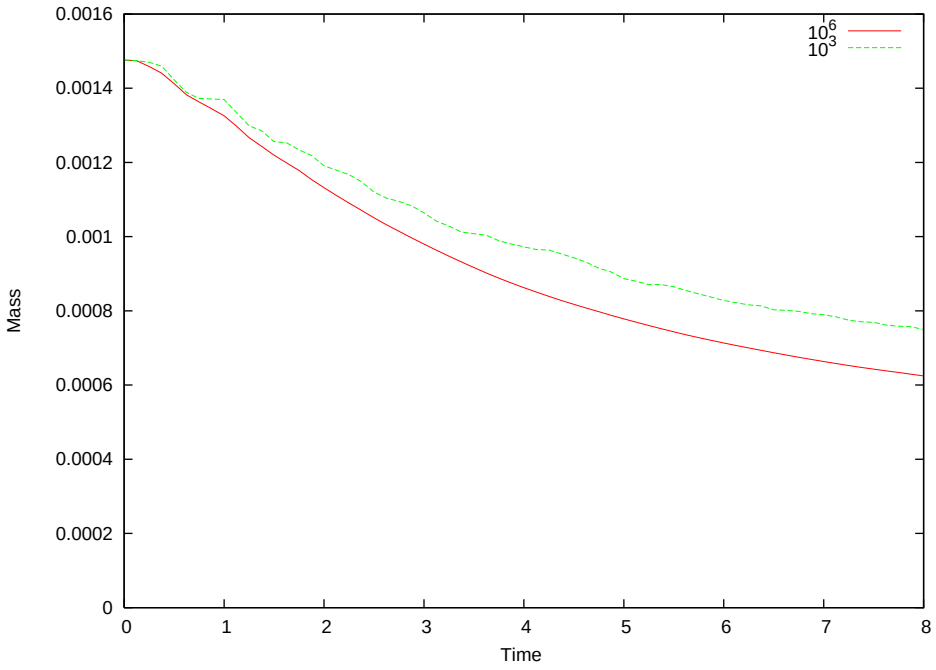
0.0016
0.0014
0.0012
0.001
0.0008
0.0006
0.0004
0.0002
0
Mass
0
1
2
3
4
5
6
7
8
Time
10^6
10^3